

# The Stellar Masses and Star Formation Histories of Galaxies at $z \approx 6$ : Constraints from *Spitzer* Observations in the Great Observatories Origins Deep Survey

Haojing Yan<sup>1</sup>, Mark Dickinson<sup>2</sup>, Mauro Giavalisco<sup>3</sup>, Daniel Stern<sup>4</sup>, Peter R. M. Eisenhardt<sup>4</sup>, Henry C. Ferguson<sup>3</sup>

## ABSTRACT

Using the deep *Spitzer* Infrared Array Camera (IRAC) observations of the Great Observatories Origins Deep Survey (GOODS), we study the stellar masses and star formation histories of galaxies at  $z \approx 6$ . The IRAC instrument provides the best opportunity to estimate the stellar masses of galaxies at these redshifts because it samples their rest-frame optical fluxes, which are less prone to dust extinction and are more sensitive to the light from longer-lived stars. Our study is based on the  $i_{775}$ -band dropout sample selected from the GOODS southern and northern fields ( $\sim 330$  arcmin $^2$  in total), several of which already have spectroscopic confirmations. In total, we derive stellar masses for 53  $i_{775}$ -band dropouts that have robust IRAC detections. These galaxies have typical stellar masses of  $\sim 10^{10} M_{\odot}$  and typical ages of a couple of hundred million years, consistent with earlier results based on a smaller sample of  $z \approx 6$  galaxies in the *Hubble* Ultra Deep Field. We also study 79  $i_{775}$ -band dropouts that are invisible in the IRAC data and find that they are typically less massive by a factor of ten. These galaxies are much bluer than those detected by the IRAC, indicating that their luminosities are dominated by stellar populations with ages  $\lesssim 40$  million years. We discuss various sources of uncertainty in the mass estimates, and find that our results are rather robust. The existence of galaxies as massive as  $10^{10} M_{\odot}$  at  $z \approx 6$  can be explained by at least one set of N-body simulations of the hierarchical paradigm. Based on our mass estimates, we derive a lower limit to the global stellar mass density at  $z \approx 6$ . Considering the range of systematic uncertainties

---

<sup>1</sup>Spitzer Science Center, California Institute of Technology, MS 220-6, Pasadena, CA 91125; yhj@ipac.caltech.edu

<sup>2</sup>National Optical Astronomy Observatory, 950 N. Cherry St., Tucson, AZ 85719

<sup>3</sup>Space Telescope Science Institute, 3700 San Martin Dr., Baltimore, MD 21218

<sup>4</sup>Jet Propulsion Laboratory, California Institute of Technology, 4800 Oak Grove Dr., Pasadena, CA 91109

in the derived stellar masses, this lower limit is  $1.1$  to  $6.7 \times 10^6 M_{\odot}$  Mpc $^{-3}$  (comoving), which is  $0.2$  to  $1.1\%$  of the present-day value. The prospect of detecting the progenitors of the most massive galaxies at yet higher redshifts is explored: a deep, wide-field near-IR survey using our current technology could possibly result in positive detections at  $z > 7$ . We also investigate the implication of our results for reionization, and find that the progenitors of the galaxies comparable to those in our sample, even in the most optimized (probably unrealistic) scenario, cannot sustain the reionization for a period longer than  $\sim 2$  million years. Thus most of the photons required for reionization must have been provided by other sources, such as the progenitors of the dwarf galaxies that are far below our current detection capability.

*Subject headings:* cosmology: observations — galaxies: evolution — galaxies: luminosity function, mass function — infrared: galaxies

## 1. Introduction

The Infrared Array Camera (IRAC; Fazio et al. 2004) of the *Spitzer Space Telescope* (Werner et al. 2004) has opened up a new window for the study of galaxies at very high redshifts. Its impressive sensitivity in the  $3.6$  and  $4.5$   $\mu\text{m}$  channels enables the detection of galaxies as distant as  $z \approx 6$ , and thus, for the first time, offers the unique opportunity of investigating the rest-frame optical properties of galaxies in the early universe. At these wavelengths, the light from a galaxy is less affected by dust extinction and is more sensitive to the longer-lived stars that dominate the stellar mass. For these reasons, IRAC observations can provide a wealth of information about the stellar population of galaxies at very high redshifts, such as their ages and stellar masses.

The past year has witnessed substantial progress in this frontier. Egami et al. (2005) used IRAC to detect a galaxy at  $z \approx 6.7$  lensed by a foreground cluster and estimated that this object has a stellar mass of  $\sim 10^9 M_{\odot}$  and is at least  $\sim 50$  Myr old. Eyles et al. (2005) discussed two field galaxies at  $z \approx 6$  that are detected in the Great Observatories Origin Deep Survey (GOODS) IRAC data and found that they are a few hundred Myr old and their stellar masses are a few  $\times 10^{10} M_{\odot}$ . Yan et al. (2005; Paper I) analyzed three galaxies at  $z \approx 6$  and 11 galaxies at  $z \approx 5$  in the *Hubble Ultra Deep Field* (HUDF) that are detected in the GOODS IRAC observations, and concluded that the observed number density of massive galaxies ( $\gtrsim 10^{10} M_{\odot}$ ) is consistent with predictions from contemporary numerical simulations of galaxy formation in a cold dark matter ( $\Lambda$ CDM) universe. Chary, Stern & Eisenhardt (2005) investigated the red IRAC color of a Ly $\alpha$  emitter at  $z = 6.56$ , and suggested that

the red color could be caused by the presence of a very strong H $\alpha$  emission line (rest-frame equivalent width  $\sim 0.2\mu\text{m}$ ) redshifted to the  $4.5\mu\text{m}$  channel. Mobasher et al. (2005) studied a galaxy in the HUDF that is not visible at optical wavelengths but is very prominent in the IRAC images, and suggested that it could be an old galaxy at  $z \approx 6.5$  with a surprisingly high stellar mass of  $5.7 \times 10^{11} M_\odot$  (but see Chen & Marzke (2004) and Yan et al. (2004) for different interpretations of this same object).

While some of the conclusions from these studies are still tentative, they show that deep IRAC observations have enabled a new perspective on studies of early galaxy formation. Previous studies, however, have been limited by the small number of galaxies that were analyzed, and by the small fields of view, where clustering variance might substantially affect space densities or other properties of the galaxy samples. In this paper, we extend the analysis to the combined areas of the two GOODS fields, in the regions of the *Hubble* Deep Field North (HDF-N) and *Chandra* Deep Field South (CDF-S). These fields cover roughly 30 times more solid angle than the HUDF alone, along two sightlines. This substantially increases the number of galaxies we can study, and should help average over variance due to large scale structure. We select F775W-band dropouts (hereafter,  $i_{775}$ -dropouts) from the *HST* Advanced Camera for Surveys (ACS) GOODS observations (Giavalisco et al. 2004a), and identify counterparts from the full-depth, two-epoch *Spitzer* IRAC observations of these fields (Dickinson et al., in preparation). These candidate  $z \approx 6$  galaxies are presented in §2 and their IRAC properties are discussed in §3. We estimate their stellar masses in §4 and discuss the implication of our results in §5. Our conclusions are summarized in §6. The magnitudes quoted in this paper are all in the AB system. Throughout the paper, we adopt the following cosmological parameters based on the first-year *Wilkinson Microwave Anisotropy Probe* (WMAP) results from Spergel et al. (2003):  $\Omega_M = 0.27$ ,  $\Omega_\Lambda = 0.73$ , and  $H_0 = 71 \text{ km s}^{-1} \text{ Mpc}^{-1}$  (our results are not affected if using the values from the three-year WMAP results for these parameters). All volumes quoted are co-moving.

## 2. Galaxy Candidates at $z \approx 6$ in the GOODS Fields

The  $z \approx 6$  galaxy candidates used in this paper are the  $i_{775}$ -dropouts selected from the complete, 5-epoch GOODS ACS observations in both the HDF-N and CDF-S (Giavalisco et al. 2004a). The selection of these candidates will be discussed in detail by Giavalisco et al. (2006, in preparation). Briefly, the selection is aimed at the redshift range of  $5.5 \lesssim z \lesssim 6.5$ , and requires a candidate have a red color across the F750W ( $i_{775}$ ) and F850LP ( $z_{850}$ ) bands, and be invisible in the F606W ( $V_{606}$ ) and F435W ( $B_{435}$ ) bands.

Quantitatively, the candidates must meet these criteria:  $S/N \geq 5$  in  $z_{850}$ ,  $(i_{775} - z_{850}) >$

1.3 mag, and  $S/N < 2$  in both the  $V_{606}$  and  $B_{435}$ . These criteria are the same as have been previously used by the GOODS team (Giavalisco et al. 2004b; Dickinson et al. 2004). While the colors are calculated based on the SExtractor (Bertin & Arnouts 1996) MAG\_ISO magnitudes, MAG\_AUTO magnitudes are used when quoting the  $z_{850}$  magnitudes of these candidates as they are closer to the “total” magnitudes. As brown dwarfs in our Galaxy have similar red colors, an “image sharpness” criterion, based on comparing peak  $z_{850}$ -band surface brightness within a  $0''.125$  aperture to the isophotal magnitude, was used to reject possible point sources from the  $i_{775}$ -dropout sample down to  $z_{850} = 26.5$  mag. This criterion was purposefully tuned to be conservative: it may improperly reject a few galaxies, but should successfully eliminate most stars down to that magnitude limit. At fainter magnitudes, it becomes difficult to robustly distinguish stars and compact galaxies in the GOODS ACS images, as the stellarity loci of stars and galaxies start to merge for any of the criteria we have considered.

After visual inspection to eliminate likely spurious sources, the resulting sample consists of 274  $i_{775}$ -dropout candidates (145 in the south, 129 in the north). Of these, eight more were further rejected as possible stars on the basis of having full-width-at-half-maximum (FWHM)  $< 0''.125$ ; two of these have been spectroscopically confirmed as stars by Vanzella et al. (2006). After this process, 142 and 124 valid candidates remain in the CDF-S and HDF-N, respectively.

We have identified five close pairs among these  $i_{775}$ -dropouts, three in the CDF-S sample and two in the HDF-N sample, respectively. The separation of the components in these pairs are all smaller than  $2''$ , which means that these pairs, if detected in the IRAC images, will be detected only as single sources (see below). Therefore, for the statistical purpose of this paper, we take the number of  $i_{775}$ -dropouts in the CDF-S and HDF-N as 139 and 122, respectively.

### 3. IRAC Detections of $z \approx 6$ Galaxy Candidates

The IRAC data used in this paper are the mosaics of the full, two-epoch data of the GOODS observations in both the CDF-S and HDF-N (Dickinson et al., in preparation; see also [http://data.spitzer.caltech.edu/popular/goods/Documents/goods\\_dataproducts.html](http://data.spitzer.caltech.edu/popular/goods/Documents/goods_dataproducts.html)). The mosaics cover approximately  $10' \times 16'$  in each field (total coverage of  $\sim 330$  arcmin $^2$ ), and have a nominal exposure time of  $\sim 23.2$  hours in each of the 3.6, 4.5, 5.8, and 8.0  $\mu\text{m}$  channels. Because of the way the observations were designed, the exposure time in the central  $\sim 20\%$  stripe of each field is twice as long. The final pixel size of the mosaics is  $0.6'' \text{ pixel}^{-1}$ , i.e., roughly half of the native IRAC pixel size. Sources were detected in a weighted sum

of the 3.6 and 4.5  $\mu\text{m}$  images using SExtractor, and their magnitudes were measured in each band through circular apertures that are 3.0" in diameter. These aperture magnitudes were converted to total magnitudes after adding aperture corrections (see Paper I). We only include sources with  $S/N > 3$  (measured in 3.6 $\mu\text{m}$  within the above mentioned aperture) for cross-matching.

The  $i_{775}$ -dropouts were cross-matched with the IRAC sources following the procedures adopted in Yan et al. (2004; 2005). As the FWHM of the point spread function (PSF) in the 3.6 $\mu\text{m}$  channel is about 1.8", the matching was done with a 2" search radius. This radius was chosen partly because of the close pairs in our sample, whose IRAC centroids are offset from those of the individual components. The matched sources were then visually inspected to ensure that the identifications were secure. In order to avoid ambiguity in interpreting the measured fluxes, we excluded any IRAC sources that are blended with neighbouring objects.

In total, 64  $i_{775}$ -dropouts have thus been securely identified in the IRAC data, with 40 in the CDF-S and the remaining 24 in the HDF-N. Among these sources, there are two pairs in the CDF-S and one pair in the HDF-N, respectively, all of which are counted as single IRAC objects in the numbers quoted above. Except for these three pairs, all other objects have their IRAC and ACS centroids matched to within 0.6", which is fully consistent with our previous experience (see Yan et al. 2004; 2005).

The Lyman-break selection of galaxies at  $z \approx 6$  is known to suffer some contamination from low-redshift, early-type galaxies that have similar red colors. Our IRAC data can be used to further reduce these contaminants. A number of the  $i_{775}$ -dropouts identified above have very bright counterparts in the IRAC images, giving flux density ratios  $f_\nu(3.6\mu\text{m})/f_\nu(z_{850}) > 20$  (or equivalently,  $(z_{850} - m_{3.6\mu\text{m}}) > 3.25$  mag). Thus they satisfy the selection criterion of the “IRAC-selected Extremely Red Objects” (IEROs; Yan et al. 2004), which are likely old, passively-evolving galaxies at  $z \approx 2.4$ . Therefore, these objects are excluded from our final sample. There are six and five such IEROs among the IRAC-detected  $i_{775}$ -dropouts in the CDF-S and HDF-N, respectively. The ratio of contamination due to IEROs is 15% for the CDF-S (six out of 40) and 21% for the HDF-N (five out of 24).

We also consider the  $i_{775}$ -dropouts that are not detected by the GOODS IRAC observations. We visually examined the IRAC images at the positions of the  $i_{775}$ -dropouts that were not cross-matched in the above procedure and found that 45 objects in the CDF-S and 34 objects in the HDF-N were undetected because of their faintness — quantitatively, they all have  $S/N < 3$  in both the 3.6 and 4.5  $\mu\text{m}$  images. The remaining 118 objects were not cross-matched because they are blended with nearby, unrelated sources.

To summarize, we are left with a final sample of 250 objects for analysis (133 in the

CDF-S and 117 in the HDF-N). We have counted the close pairs as single sources, and have excluded the possible contaminants (brown dwarfs and IEROs). The final sample of  $i_{775}$ -dropouts that are securely detected in the IRAC data has a total of 53 objects (34 in the CDF-S and 19 in the HDF-N). The 3.6  $\mu\text{m}$ -band magnitudes of these objects range from 23.27 to 26.50 mag. The final sample of  $i_{775}$ -dropouts undetected in the IRAC data consists of 79 objects (45 in the CDF-S and 34 in the HDF-N). In the rest of the paper, we will refer to these two samples as the “IRAC-detected sample” and the “IRAC-invisible sample”. The remaining 118  $i_{775}$ -dropouts (54 in the CDF-S and 64 in the HDF-N) are blended with unrelated neighbours. IEROs make up  $\sim 17\%$  of the non-blended sample, and it is plausible that the same fraction also holds in the blended sample. Therefore, a total of 98 objects in the blended sample could be galaxies at  $z \approx 6$  after excluding this fraction of IERO contamination. We will refer to the sample of these 98 objects as the “blended sample”.

Despite that we have utilized every means to eliminate various sources of contamination, our final sample could still have some contaminants. This is particularly possible among the objects of low  $S/N$ , where spurious sources are more likely to occur and low-redshift, red galaxies (not necessarily as extreme as the IEROs) are more easily scattered above the color selection threshold. To address this issue, we use the much deeper ACS data in the HUDF to assess the quality of our candidate selection. Thirteen objects in our CDF-S candidate list are within the coverage of the HUDF, and all of them are verified to be real objects. Therefore, the contamination caused by spurious sources seems to be negligible to the  $S/N$  level that we consider. However, three of these thirteen sources are not among the HUDF  $i_{775}$ -dropout list of Yan & Windhorst (2004b). These three sources ( $S/N \approx 5$  in the GOODS data) have  $i_{775} - z_{850} < 0.5$  mag in the deeper HUDF data, indicating that the contamination rate in our final sample caused by photometric error could be as high as  $\sim 23\%$ . We will take this into account when discussing the implications of our results in §5.

Fig. 1 shows the  $z_{850}$ -band magnitude distributions of the IRAC-detected and IRAC-invisible samples as histograms of different colors. Their median magnitudes are 26.32 and 27.00 mag, respectively. For comparison, the median magnitude of the blended sample is 26.71 mag. While the objects in the IRAC-invisible sample are fainter on average, the majority of them are still within the range of the IRAC-detected sample.

#### 4. Constraining the Stellar Masses of $z \approx 6$ Galaxies

In this section, we constrain the stellar masses of  $z \approx 6$  galaxies in both the IRAC-detected and the IRAC-invisible samples as defined in §3. For this purpose, we compare our observations to the stellar population synthesis models of Bruzual & Charlot (2003; hereafter

BC03). As per Paper I, we explore the models of the following star formation histories (SFHs): instantaneous bursts (or Simple Stellar Populations, SSPs), and continuous bursts with exponentially declining star formation rate (SFR) in the form of  $SFR \propto \tau^{-1} \exp(t/\tau)$ , where the time-scale  $\tau$  ranges from  $\tau = 10$  Myr to 1 Gyr. The step size in  $\tau$  is 10 Myr for  $\tau = 10$  Myr to 0.1 Gyr, and is 0.1 Gyr for  $\tau = 0.1$  to 1 Gyr. For each of these SFHs, we generate models with ages ranging from 1 Myr to 1 Gyr; the step size in age is 10 Myr when the age is less than 0.1 Gyr, and is 0.1 Gyr when it ranges from 0.1 to 1 Gyr. To facilitate comparison to other, published studies, we use a Salpeter initial mass function (IMF; Salpeter 1955) extending from 0.1 to  $100 M_\odot$ . Many recent studies indicate that the actual IMF in most environments probably has fewer low-mass stars ( $< 1 M_\odot$ ) than are predicted by the Salpeter IMF power-law slope (e.g., Kroupa 2001; Chabrier 2003). These stars contribute very little to the observed light from galaxies, and therefore, to first order, changing the low-mass IMF simply rescales all masses and star formation rates derived from comparison to stellar population models. Generally speaking, using a Chabrier IMF would lower the mass estimates by about 50–60%. Changes to the IMF shape and slope at higher masses, however, may lead to wavelength-dependent and time-dependent changes in the mass-to-light ratios ( $M/L$ ) relative to the assumed Salpeter models.

In Paper I, we carried out detailed SED analysis using models of different metallicities and various reddening values, and allowed the redshift be a free parameter when it was unavailable. When single-component models did not fit well, we also considered two-component models. Here, however, it is difficult to take this approach, because the objects in the IRAC-detected sample are only significantly detected in two to three passbands ( $z_{850}$  and  $3.6\mu\text{m}$ , some are also detected in  $4.5\mu\text{m}$ ). This is particularly true for the IRAC-invisible objects, as they are only significantly detected in one band ( $z_{850}$ ). Therefore, we have to use a different method, detailed below. We will mainly concentrate on models of solar metallicity and zero reddening, but will also discuss the effects of different metallicities and reddening values.

Currently, seven objects in the IRAC-detected and -invisible samples have already been spectroscopically confirmed at  $z > 5.5$  (Stanway et al. 2004a, 2004b; Dickinson et al. 2004; Vanzella et al. 2006; Stern et al., in preparation; Vanzella et al., in preparation). For the sake of simplicity, however, we choose to assign a common redshift of  $z = 6$  for all objects. We will discuss the bias caused by this simplification in §4.3 together with other sources of uncertainty.

#### 4.1. Stellar Masses of IRAC-Detected Objects

For each object, we first examine how its luminosity in the IRAC bands constrains the upper limit of its stellar mass. The luminosity of an object with fixed mass is determined by its age and SFH, and becomes fainter as it gets older; i.e., its  $M/L$  becomes larger as it evolves. It can reach the largest possible  $M/L$  if it forms all its stars through an instantaneous burst and passively evolves to its maximal age (i.e., a SSP; see Fig. 2). Therefore, an object can have the highest possible mass (assuming no dust extinction) if its luminosity is dominated by such a “maximally old”, single-burst component. This methodology is similar to that adopted in Papovich et al. (2001). In practice, we assume that all the flux of an object detected in the  $3.6\mu\text{m}$  channel comes from this maximally old component. The  $3.6\mu\text{m}$  channel is chosen because it has the highest sensitivity of the IRAC bands, and thus the measurements in this channel have the highest S/N. As we assume the objects in our sample are all at  $z = 6$ , their maximal age allowed (i.e., setting the formation redshift  $z_f = \infty$ ) in our adopted cosmology is 0.95 Gyr. To match the model grid in age domain, we take their maximal ages as 1.0 Gyr. The stellar mass upper limit of a given object is then obtained by comparing its  $3.6\mu\text{m}$  magnitude to the prediction given by the 1.0 Gyr-old SSP model. Hereafter we refer to this limit as “ $M_{\max}$ ”, and the method as the “maximally-old component method”<sup>5</sup>.

Next, we find the lower bound to the stellar mass (hereafter  $M_{\min}$ ) of each object. If the SFH of an object is known, its  $(z_{850} - m_{3.6\mu\text{m}})$  color can be used as an indicator of its age (see Fig. 3). Its mass can be derived through comparison of the observed  $3.6\mu\text{m}$  magnitude to the prediction of the corresponding model at the inferred age. As we do not know what SFH a given object has, we consider the full range of models and obtain one mass estimate for each model. For each galaxy, the minimum among all these estimates is taken as its  $M_{\min}$ .

Given our assumptions, the true mass of a galaxy will lie between  $M_{\min}$  and  $M_{\max}$ . While there is no other information that can further help us judge what its true mass might be, we use the median mass from the set of exponential SFH models fitted to match the

---

<sup>5</sup> Assuming no dust extinction (discussed in §4.3), the  $M_{\max}$  value thus obtained marks a firm upper limit to the mass. The maximally-old component always underpredicts the flux in  $z_{850}$ -band, and to explain the observed  $z_{850}$ -band flux would require a secondary, young component be added. In such a two-component, “old+young” model, the derived mass of a galaxy will be smaller than the  $M_{\max}$  value that we obtained, because the contribution from the young component will reduce the  $M/L$ . The exact amount of such a reduction depends on the assumed age and SFH of the young component; using the suite of models shown in Fig. 3 for this young component, the derived maximum mass will be smaller than our current  $M_{\max}$  value by a few to 50% on average. As we have no further constraints on the young component, we choose to adopt the  $M_{\max}$  value based on our current simplistic model as a safe upper limit.

$(z_{850} - m_{3.6\mu m})$  color. We refer to this as the “representative mass” of this galaxy (hereafter  $M_{\text{rep}}$ ). We also refer to the age corresponding to this  $M_{\text{rep}}$  as its “representative age” ( $T_{\text{rep}}$ ). The representative masses range from  $0.09\text{--}7.0 \times 10^{10} M_{\odot}$  (the median is  $9.5 \times 10^9 M_{\odot}$ ) and the representative ages range from 50–400 Myr (the median is 290 Myr); both are consistent with one of the general conclusions in Paper I that some galaxies as massive as a few  $\times 10^{10} M_{\odot}$  were already in place at  $z \approx 6$ , and that they are typically a few hundred million years old. The histograms of the three values,  $M_{\text{min}}$ ,  $M_{\text{rep}}$  and  $M_{\text{max}}$ , are shown in the top panel of Fig. 4. As a further justification of using  $M_{\text{rep}}$  and  $T_{\text{rep}}$ , we note that  $M_{\text{rep}}$  for J033240.01-274815.0 is  $2.1 \times 10^{10} M_{\odot}$ , which is well within a factor of two of the best-fit mass of  $3.4 \times 10^{10} M_{\odot}$  that Paper I derived for this object using a more sophisticated SED analysis. For comparison, the  $T_{\text{rep}}$  value of this object is 200 Myr, while the analysis of Paper I shows that the evolved component of this object has an age of 500 Myr.

#### 4.2. Stellar Masses of IRAC-Invisible Objects

The fact that many objects are undetected in the IRAC data immediately suggests that they are likely much less massive than the IRAC-detected ones. The  $3.6\mu m$  flux density upper limits of these sources, measured as  $2\sigma$  fluctuation within a  $3''$ -diameter aperture, range from 0.029 to  $0.091 \mu\text{Jy}$  (27.73 to 26.50 mag), with the median of  $0.042 \mu\text{Jy}$  (27.35 mag). Using the maximally-old-component method described above, we derive the stellar mass upper limits of these objects based on their flux density upper limits. Again, we assume all galaxies are at  $z = 6$ . These upper limits, which are shown in the dotted histogram displayed in the lower panel of Fig. 4, range from  $3.0\text{--}9.4 \times 10^9 M_{\odot}$ . The median of these *upper limits* is  $4.3 \times 10^9 M_{\odot}$ , which is not only less than the upper limit of the IRAC-detected sample in general, but is also significantly less than the median of the *representative mass* of the latter by a factor of two.

Fig. 5 compares the  $(z_{850} - m_{3.6\mu m})$  colors of the IRAC-detected objects (red squares) with the upper limits of these colors of the IRAC-invisible objects (downward arrows)<sup>6</sup>. This comparison suggests that the IRAC-invisible objects are not only less massive than the IRAC-detected ones but are also bluer on average, indicating that young stellar populations are playing a dominant role — by luminosity — in these galaxies.

---

<sup>6</sup>The “gap” in this figure that seemingly separates the IRAC-detected and IRAC-invisible objects does not imply that these are two distinctly different populations. Instead, the transition between these two samples should be rather smooth. The “gap” is largely caused by the sources that fall just slightly below our detection threshold in IRAC ( $S/N > 3$ ), whose  $(z_{850} - m_{3.6\mu m})$  color limits are then calculated by using their  $2\sigma$  flux upper limits in the  $3.6\mu m$ -band.

To further test the robustness of the conclusion that these objects are less massive, we stacked their  $3.6\mu\text{m}$  images to increase the S/N of the detection. For each object, a  $12.6'' \times 12.6''$  section (i.e., 21-pixel on a side) around its center was cut out from the  $3.6\mu\text{m}$  image. We then combined these image “stamps” together by taking their median value at each pixel. We adopted median rather than average as the stacking algorithm, because the former is more effective in rejecting the contaminating pixels from the neighbours around invisible sources. The final median stack is displayed in the left panel of Fig. 6, which shows a visible, albeit weak, source at the center (see pixels within the circle). For comparison, the right panel of this figure shows the stack of the same number of randomly chosen image stamps, where no detectable source at the center can be seen.

This weak source represents the average property of the IRAC-invisible  $i_{775}$ -dropouts in the  $3.6\mu\text{m}$  channel. To extract its flux, we utilized a  $1.2''$ -diameter (2 pixels) aperture. The background value and the aperture correction to total flux were determined through simulation. The simulation was performed for 20 runs, and in each run 830 different artificial galaxies with a total magnitude of 27.50 mag were randomly distributed over the real image. Image stamps of these artificial galaxies (16,600 in total) were cut out and stacked in the same way as we stacked the IRAC-invisible sources. The peak value of the pixel histogram of this stack was chosen as the background value, and the magnitude of the stacked artificial galaxy was extracted using a  $1.2''$ -diameter aperture. The aperture correction was calculated as the difference between this aperture magnitude and the input total magnitude. The same background value and the aperture correction were then applied to the real stack of the IRAC-invisible object. Its total magnitude thus obtained is 27.44 mag, which is consistent with the flux density upper limits described above.

By the same token, the representative property of this median IRAC source in  $z_{850}$ -band can be described by the median  $z_{850}$  magnitude of the IRAC-invisible sample, which is 27.00 mag. Using the same analysis in §4.1, we obtain  $(M_{\min}, M_{\text{rep}}, M_{\max})$  estimates for a typical source in the IRAC-invisible sample as  $(1.5 \times 10^8, 2.0 \times 10^8, 5.9 \times 10^9) M_{\odot}$ . For all three types of estimates, the masses derived from the median-stack photometry are much smaller than those for the objects in the IRAC-detected sample (see the dashed lines in the top panel of Fig. 4). The  $T_{\text{rep}}$  value of this median source is 30 Myr.

### 4.3. Sources of Uncertainty in Mass Estimates

A major source of uncertainty is in the systematic of the measurement of the  $(z_{850} - m_{3.6\mu\text{m}})$  color. As it is used as the age estimator, this color affects both  $M_{\min}$  and  $M_{\text{rep}}$  (but not  $M_{\max}$ ). In this study, we use total magnitude for  $m_{3.6\mu\text{m}}$  and SExtractor MAG\_AUTO

for  $z_{850}$ . Although MAG\_AUTO is frequently taken to represent the total magnitude of a galaxy, in practice it may be subject to biases, particularly for faint objects in high-resolution *HST* images. Monte Carlo simulations of photometry for artificial objects in the GOODS ACS images indicates that at the typical magnitudes of our  $i_{775}$ -dropouts, the MAG\_AUTO magnitude underestimates the total  $z_{850}$ -band flux of an object by  $\sim 0.5$  mag. This means that the true  $(z_{850} - m_{3.6\mu m})$  color could be 0.5 mag bluer than our current estimate, and thus the age of a given object could be younger, and hence the  $M/L$  could be smaller. We find that our current  $M_{\min}$  and  $M_{\text{rep}}$  values could have been overestimated by  $\sim 21\%$  if the  $(z_{850} - m_{3.6\mu m})$  color is indeed 0.5 mag bluer than we adopted.

In addition to photometry, there are more complicated sources of uncertainty. When deriving the results shown in previous sections, we have made three major simplifications, namely, the galaxies (or equivalently, the models) are all at  $z = 6$ , all have solar abundance and all are free of dust obscuration. Here we discuss the systematics introduced by such simplifications. We mainly discuss the effects on the derived stellar mass, as our current study largely concentrates on this quantity. We consider how the derived masses would change if we vary the assumed values for the redshift, metallicity, and reddening. We express the systematics in terms of relative difference in mass,  $\Delta M^i/M$ , where the superscript  $i$  can be “ $z$ ” (redshift), “Fe/H” (metallicity) and “red” (reddening). The quantity  $\Delta M$  is defined as  $\Delta M = M - M'$ , where  $M$  is the value obtained using our adopted models, and  $M'$  is the value obtained when the model parameter in question is changed. A positive value of  $\Delta M^i/M$  indicates that our default models yield a larger estimate for the mass than those where parameter  $i$  is changed, and a negative value means the opposite. We consider the effects of model parameter changes on all three mass estimates considered here, namely,  $M_{\min}$ ,  $M_{\text{rep}}$ , and  $M_{\max}$ . We only discuss the IRAC-detected sample, but the conclusions could similarly be applied to the IRAC-invisible sample.

By fixing the redshift, we ignore the differences in the redshifted SED, in the luminosity distance, and in the amount of the IGM absorption. The first two factors (especially the luminosity distance) are the most relevant in deriving  $M_{\max}$  using a maximally-old SSP. Using a  $z = 6$  SSP will overestimate the  $M_{\max}$  values for objects at lower redshifts, and will underestimate them for objects at higher redshifts. This is demonstrated in the bottom panel of Fig. 7 for two extreme cases of  $z = 5.5$  (asterisks) and  $z = 6.5$  (open squares). The  $M_{\max}$  values of our objects in the IRAC-detected sample have been recalculated using a SSP at  $z = 5.5$  and a SSP at  $z = 6.5$ , respectively. Our original values would overestimate by 21% if the objects were actually all at  $z = 5.5$ , and would underestimate by 27% if they were actually all at  $z = 6.5$ .

For galaxies at  $z \gtrsim 5.9$ , the Ly $\alpha$  forest suppresses the flux detected in the  $z_{850}$ -band.

This has no effect on the maximal mass estimates,  $M_{\max}$ , which is based only on the flux in the  $3.6\mu\text{m}$  channel. However, it does impact the mass estimates  $M_{\min}$  and  $M_{\text{rep}}$ , which make use of  $M/L$  derived from the  $z_{850}$ - $3.6\mu\text{m}$  color. For example, if the object under question is actually at  $z > 6$ , its observed  $(z_{850} - m_{3.6\mu\text{m}})$  color would be redder than what is expected when at  $z = 6$ , because its flux in the  $z_{850}$ -band is more severely suppressed. Applying a  $z = 6$  template to such a color will result in an artificially older age (see Fig. 3), and hence an artificially larger  $M/L$  (see Fig. 2). As a result, both  $M_{\min}$  and  $M_{\text{rep}}$  will be overestimated. This overestimate, however, is partially canceled by the change in the luminosity distance and the  $k$ -correction. The top and middle panels of Fig. 7 show that the assumption of  $z = 6$  would overestimate  $M_{\min}$  and  $M_{\text{rep}}$  by about 25% for galaxies that were in fact at  $z = 6.5$  (see the open squares). At  $z < 6$ , this effect results in underestimates. However, as the change of the IGM opacity across the  $z_{850}$ -band is negligible at this redshift regime, the mass estimates change by only a few percent if the galaxies were instead at  $z = 5.5$ . This is shown in the top and middle panels of Fig. 7 as asterisks.

In Paper I, we considered the metallicities varying from solar abundance to 1/200 of solar, the latter being the smallest value available from the BC03 models. We found that the  $z \approx 6$  objects in the HUDF are usually best fitted by models with solar abundance. For this reason, we have adopted the simplifying assumption of solar metallicity for our fiducial models. As it is not likely that objects in the early universe would have higher abundance, here we only examine the extreme case at the low metallicity end, i.e., how our results would be biased if all the objects actually have their abundance of 1/200 of solar. Fig. 8 shows the relative differences of the three mass estimates, all evaluated at  $z = 6$ . Models with subsolar metallicites generally have bluer colors at a fixed age; hence, older ages are required to match the observed colors, and this leads to larger  $M/L$ . Therefore, the masses based on the colors ( $M_{\min}$  and  $M_{\text{rep}}$ ) derived using the solar abundance models are smaller than those derived from models with  $Z = Z_{\odot}/200$  by 70% and 32%, on average. For  $M_{\max}$ , instead, the solar abundance models have higher  $M/L$ , and hence the masses are 32% larger than those for models with 1/200th solar metallicity.

Dust reddening and obscuration will also affect the derived masses. In Paper I, we found that the best-fit models always have near-zero reddening, although an amount up to  $E(B - V) = 0.4$  to 0.5 mag could not be excluded. This is because we had to account for the very blue rest-frame UV colors observed for the galaxies studied in that paper, which we did by invoking two-component models with both younger and older stars. The best-fit models always have  $E(B - V) \approx 0$  if we require both components to have the same reddening. However, if this *ad hoc* requirement is removed, the reddening becomes unconstrained. Here, we consider the effects of non-zero reddening on our results. For mass estimates based on a color measurement, i.e.,  $M_{\min}$  and  $M_{\text{rep}}$ , the effects of reddening and age on  $M/L$  derived

from the models tend to cancel, resulting in relatively small changes in the final derived masses. Dust makes the observed  $3.6\mu\text{m}$  flux fainter, thus increasing  $M/L$ . However, it also reddens the spectrum, requiring a younger model to match the observed ( $z_{850} - 3.6\mu\text{m}$ ) color, and this younger model will have an intrinsically smaller  $M/L$  (before applying the extinction). For illustration, we consider the effects of  $E(B - V) = 0.2$  mag of extinction, assuming the attenuation law of Calzetti et al. (2000). The results are shown in Fig. 9. Although this reddening corresponds to nearly 1 mag of extinction in the observed  $3.6\mu\text{m}$  band and more than 2 mag at  $z_{850}$ , the average change in the derived  $M_{\min}$  and  $M_{\text{rep}}$  is only 13% and 30% (overestimated), respectively, as the model age changes to compensate the extinction.  $M_{\max}$ , on the other hand, is derived from the photometry at  $3.6\mu\text{m}$  alone, and hence changes by a factor of 3.3 (underestimated).

In the end, we find that most of our mass estimates are relatively robust against large changes in the values assumed for the redshift, metallicity, and extinction. In most cases, varying those parameters over the ranges described here, the derived masses change by less than 35%. If metallicity were as low as 1/200th solar, then our values for  $M_{\min}$  (derived assuming  $Z_{\odot}$  models) would be underestimated by 70% on average. The largest effect would be that of reddening on our estimates of  $M_{\max}$ , which could be increased by a large factor if reddening were substantial. However, we note that this would imply substantial reddening on the old (1 Gyr) stellar population assumed in the toy model from which the mass upper limits are derived. In practice, the mass could be increased arbitrarily by adding dust to an old stellar population, but such a model seems rather arbitrary and unphysical, and also fails to take into account the observed UV light and UV-to-optical rest-frame colors of the galaxies. Instead, the mass estimates derived from the observed colors ( $M_{\min}$  and  $M_{\text{rep}}$ ) are comparatively insensitive to reddening. Other stellar population properties are more sensitive to these systematic effects. In particular, both age and SFR are completely degenerate with extinction when only a single color is used for analysis. Thus, while we have shown that the mass estimates are comparatively robust, other properties are more uncertain, and rely more heavily on the inference for low extinction from more detailed analysis of the smaller HUDF sample in Paper I.

#### 4.4. Legitimacy of Adopted Declining SFHs

The stellar mass estimates that we obtained in this study hinge upon the exponentially declining SFHs that we assumed. Such SFHs imply that the star-formation activities of these objects were more intense in the past than in the epoch when they are observed. While it is impossible to directly verify this picture based on our current data, we can at least test

if our results are self-consistent with the assumption that the SFHs of these objects are a declining function of time.

One quantity that can be used to address this question is “specific SFR”, which is defined as the ratio of the current SFR and the total stellar mass. The reciprocal of this quantity is the period of time (denoted as  $\tilde{T}$ ) during which a galaxy could build up its total mass if it were maintaining the same, constant SFR in the past. The current SFR can be calculated according to eqn. 2 of Madau, Pozzetti & Dickinson (1998), i.e.,  $L_{UV} = 8.0 \times 10^{27} \times SFR$ , where  $L_{UV}$  is the flux (in ergs/s/Hz) at rest-frame 1500Å. The SFR thus derived is insensitive to the past SFH when the age of the galaxy is much longer than the life time of O and B stars at the main sequence. We convert the  $z_{850}$ -band magnitudes to  $L_{UV}$ , again assuming that the objects are all at  $z = 6$ , and ignoring the caveat that the  $z_{850}$ -band actually samples the continuum at around 1300Å.

Fig. 10 shows the specific SFR (calculated by dividing the  $M_{rep}$  into the SFR value) of the IRAC-detected sample as the function of stellar mass (solid triangles). The result for the median-stack of the IRAC-invisible objects is also plotted (the asterisk). The data points form a tight sequence that is between constant SFR of 3.0 and  $30 M_{\odot} \text{yr}^{-1}$ , which are shown as the two straight lines to the left and right, respectively. This primarily reflects the rest-frame UV magnitude range of the sample ( $24.9 < z_{850} < 27.4$  mag) and its conversion into star formation rates ( $30 > SFR/(M_{\odot} \text{yr}^{-1}) > 3$ ). The lower envelope in specific star formation rates corresponds to the  $z_{850}$  magnitude limit of the sample. The upper envelope may have greater physical significance, corresponding to the high-luminosity cut-off in the UV luminosity function for galaxies at  $z \approx 6$ .

The  $\tilde{T}$  values are much larger than the representative galaxy ages,  $T_{rep}$ , obtained in the previous section. More than half of these objects (58%) have  $\tilde{T}$  larger than the age of the universe at  $z \approx 6$  (some are even  $> 4$  Gyr), which is a clear indication that there would not have been sufficient time for them to acquire their masses if their past SFRs were as low as their current values. In other words, their SFRs must have been declining and must be much larger in the past, which is consistent with the assumed models.

One caveat of the discussion above, however, is the possible role of dust extinction. If the galaxies in our sample suffered a reddening of  $E(B-V) = 0.2$  mag (as discussed in §4.3), their true ongoing SFR would be higher than the current estimates by a factor of  $\sim 8.5$ , and yet their  $M_{rep}$  values would be lower by  $\sim 30\%$  (see §4.4). As a result, their  $\tilde{T}$  values would be smaller by a factor of  $\sim 12$ , and hence the majority of them could still build up their stellar masses within the time allowed by the age of the universe. However, even in this case, the  $\tilde{T}$  values (with the median of 155 Myr) are still much larger than  $T_{rep}$  derived based on the reddened models (with the median of 10 Myr). Therefore, this is still consistent with

our assumption that the objects in our sample have higher SFRs in the past.

## 5. Cosmological Implications

The results presented above show that some galaxies as massive as a few  $\times 10^{10} M_{\odot}$  were already in place by  $z \approx 6$ , and that their typical ages are a few hundred million years old, which are consistent with our earlier results in Paper I. In this section, we discuss the cosmological implications of these results.

### 5.1. Comparison to $\Lambda$ CDM Simulations

Following Paper I, here we further investigate how well the observed number density of very massive galaxies at  $z \approx 6$  can be explained by the numerical simulations of the hierarchical paradigm. As in Paper I, we make comparison to the mass functions (MF) predicted by two types of hydrodynamic simulations in a  $\Lambda$ CDM universe, namely, a Smoothed Particle Hydrodynamics (SPH) simulation and a Total Variation Diminishing (TVD) simulations (Nagamine et al. 2004; Night et al. 2006). The simulation box sizes are  $100h^{-1}$  Mpc and  $22h^{-1}$  Mpc, respectively. The cumulative MF from these two simulations are given in Fig. 11. As the simulation volume is not unlimited, both MF are cut-off at the high-mass end (at around  $1.8 \times 10^{11}$  and  $2.0 \times 10^{10} M_{\odot}$  for the SPH and TVD models, respectively). Nevertheless, comparing to these models is still meaningful, as they extend to the regime where our observations are rather complete. For reasons as described in detail in Paper I, our IRAC data should be complete for detecting galaxies with  $M > 1.6 \times 10^{10} M_{\odot}$ , which is indicated in the figure as the vertical dotted line.

In Paper I, we derived a lower limit for the cumulative number density above the same mass threshold, which is  $8.0 \times 10^{-5}$  Mpc $^{-3}$ , and we concluded that the predictions from the SPH and TVD simulations were a factor of  $2.6 \times$  and  $4.6 \times$  larger than this lower limit. However, we recently discovered that the mass functions from the SPH and TVD simulations were presented with incorrect normalization in Paper I, leading to predicted number densities that were too high by a factor of 6.0 and 3.8, respectively. Using the corrected numbers, the SPH and TVD predictions should be  $0.4 \times$  and  $1.2 \times$  of the observed lower limit.

As the sample in Paper I is very small (three objects), the much larger sample in our current study offers a better statistics for comparison. Using the redshift selection function for our color criteria, which we evaluate from Monte Carlo simulations following the procedures described in Giavalisco et al. (2004b), we obtain the effective volume of

$8.0 \times 10^5 \text{ Mpc}^3$  for our  $i_{775}$ -dropout sample. The cumulative number densities inferred from the  $(M_{\min}, M_{\text{rep}}, M_{\max})$  values of the IRAC-detected sample are shown as the blue, yellow and red solid curves, respectively. If we assume that the stellar mass distribution of the blended sample is the same as the non-blended sample, we can obtain the total contribution from the combined non-blended and blended samples by scaling the results that we obtained for the non-blended sample. This scaling factor is 1.74. The dot-dashed curves in Fig. 11 show the observed number density after this correction being applied, and are what will be used to compare to the models. The flattening of the observed curves at lower masses is a consequence of increasing incompleteness at fainter magnitudes.

At the mass threshold of  $M > 1.6 \times 10^{10} M_{\odot}$ , the cumulative number density derived from our observations is  $(2.6, 4.7, 10.6) \times 10^{-5} \text{ Mpc}^{-3}$  based on  $(M_{\min}, M_{\text{rep}}, M_{\max})$ , respectively. The SPH model prediction is  $\sim 1.3 \times$ ,  $0.7 \times$  and  $0.3 \times$  of the observations. The TVD model prediction, on the other hand, is  $\sim 3.7 \times$ ,  $2.1 \times$  and  $0.9 \times$  of the observations. This comparison shows that the number density of the observed high mass galaxies agrees reasonably well with the models to within the uncertainty of the stellar mass estimates. The prediction from the TVD model is considerably higher than that from the SPH model, which reflects the uncertainty in simulations caused by the differences in the implementation methods, such as the mass and spatial resolutions, the simulation box sizes, and the initial conditions (Nagamine, priv. communications). In particular, the smaller box size of the TVD simulation has a significant impact at the high-mass end, as the statistics is dominated by only a small number of objects (only 2–3 galaxies above our chosen mass threshold). Nevertheless, the comparison between our observations and these simulations does show that the models of the hierarchical paradigm are capable of producing sufficient number of high mass galaxies at the early epoch stage of the universe.

## 5.2. Global Stellar Mass Density

Based on the stellar masses obtained for our sample, here we estimate the global stellar mass density at  $z \approx 6$ . To address this question, ideally one would need a mass-limited, complete sample. However, the  $i_{775}$ -dropout sample that we have been using is not mass-limited. Since it was selected from the rest-frame UV luminosities of the objects, which do not correlate directly with stellar masses. While the incompleteness of this sample can be quantified as a function of rest-frame UV luminosity, this cannot easily be transferred to the mass-domain. In fact, the discussion in §5.1 suggests that our sample could possibly suffer from significant incompleteness even at the high-mass end. Nevertheless, we can still use our current sample to constrain the lower limit of the global stellar mass density at  $z \approx 6$ .

Adding the  $(M_{\min}, M_{\text{rep}}, M_{\max})$  estimates of the individual objects in the IRAC-detected samples, the total stellar mass density locked in these galaxies is  $(5.8, 9.1, 31.4) \times 10^5 M_{\odot} \text{Mpc}^{-3}$ . The contribution inferred from the IRAC-invisible samples is much smaller. The total stellar mass contributed by this sample can be approximated by multiplying the total number of objects to the stellar mass estimates of the median stack described in §4.2, which corresponds to stellar mass density of  $(0.14, 0.20, 5.9) \times 10^5 M_{\odot} \text{Mpc}^{-3}$ . Therefore, the sum of both samples is  $(5.9, 9.3, 37.3) \times 10^5 M_{\odot} \text{Mpc}^{-3}$ . We also correct for the incompleteness caused by crowding by considering the IRAC-blended sample in the same way as in §5.1 (i.e., multiplying by a factor of 1.74). The final stellar mass density after this correction is  $(10.4, 16.3, 64.8) \times 10^5 M_{\odot} \text{Mpc}^{-3}$ .

This result is shown in Fig. 12, together with the estimates at lower redshifts (Dickinson et al. 2003). The data are shown in terms of ratios to the critical mass density, which is  $1.4 \times 10^{11} M_{\odot} \text{Mpc}^{-3}$  in our adopted cosmology. We note that, however, these results have not yet taken into account the fact that our  $i_{775}$ -dropout sample could still be contaminated by low-redshift galaxies that are not as extreme as the IEROs (see §3). Considering this effect, the results presented above could be reduced by  $\sim 23\%$ .

Finally, we emphasize that, while the objects in our IRAC-invisible sample make a small contribution to the total stellar mass density, this does not necessarily mean that the less massive galaxy population only makes up an insignificant fraction of the total stellar mass density at  $z \approx 6$ . If the MF of galaxies at  $z \approx 6$  has a very steep slope at the low-mass end (see Fig. 11), the contribution from the less massive galaxies that are missing from our IRAC data could be much higher than that from the galaxies at the high-mass end.

### 5.3. Progenitors of High-mass Galaxies: Detectability at $z > 7$

In §4.4, we argue that the objects in the IRAC-detected sample should have much higher SFRs in the past. This implies that the progenitors of these objects were once much more UV-luminous than they are at  $z \approx 6$ . Since there have already been some efforts to push the current redshift boundary to  $z > 7$  (e.g., Bouwens et al. 2004), it is relevant to discuss the prospect of detecting such early galaxies from a different perspective.

Consider a typical object in the high-mass subset of the IRAC-detected sample that has  $M_{\text{rep}} = 2.0 \times 10^{10} M_{\odot}$ . The stellar mass and the instantaneous SFR that its progenitor has at a given age depend on its SFH, as does its luminosity. Using the BC03 models that we adopt, we predict the apparent magnitude of its progenitor at any given redshift for a range of formation and observed redshifts. Fig. 13 shows two examples by assuming  $z_f = 7.8$  (top

panel) and  $z_f = 9.0$  (bottom panel), and gives its apparent magnitude in  $J$ -band if it is observed 50 Myr (blue) and 100 Myr (red) after the birth. We choose these two formation redshifts for demonstration because the age of the object when evolving to  $z \approx 6$  would be  $\sim 200$ –400 Myr, which is within the range of  $T_{\text{rep}}$  of the objects in the high-mass subset. In most models that we consider, the progenitor of such a very massive object should be detected at  $J \approx 24$  mag. Based on the number of similar objects in the IRAC-detected sample, the surface density of such progenitors would be  $\sim 0.05 \text{ arcmin}^{-2}$ . While it is too low for the existing deep, pencil-beam surveys using the Near Infrared Camera and Multi Object Spectrometer onboard the *HST* (e.g., Thompson et al. 1999, 2005; Dickinson et al. 2000; Bouwens et al. 2004, 2005), such a surface density is high enough to produce a significant number of detections through a deep survey over a few hundred  $\text{arcmin}^2$  that is now feasible using the new generation of wide-field near-IR instruments at ground-based observatories.

This simple argument echos the ones made about three decades ago regarding the progenitors of the local giant ellipticals, when it was suggested that such progenitors (“primeval galaxies”) could have formed most of their stars within a short period of time and thus their rest-frame UV luminosities could be so high that they could be easily detected at very high redshifts (e.g., Partridge & Peebles 1967; Sunyaev, Tinsley & Meier 1978; Shull & Silk 1979). Even at that time, however, it was realized that dust extinction could easily quench the UV fluxes and thus those progenitors might not be as bright as expected (e.g., Kaufman 1976). The same is also true in our discussion here. For example, a modest amount of dust equivalent to a reddening of  $E(B-V) \approx 0.2$  mag could easily suppress our predicted  $J$ -band brightness by more than 2 magnitudes, and therefore would make the detection of such progenitors at  $z > 7$  much more difficult. A null detection from a deep, wide-field survey would still be valuable, however, as it could then be used to constrain how dusty the very early galaxies could be and shed new light to their forming mechanism.

There is another factor that could affect the detectability of the progenitors of high-mass galaxies. If the high-mass objects that we see at  $z \approx 6$  are the merger products of many much less massive progenitors, the luminosity of an individual progenitor could be much fainter and escape detection. In this case, a null detection would imply a high merger rate within the first several hundred million years of the universe, which would provide some constraints on the hierarchical formation theory.

#### 5.4. Implication for Reionization

As it is possible that the high-mass galaxies were born through very intense star-formation processes, it is interesting to study the role of their progenitors in reionizing the neutral hydrogen in the early universe. Specifically, here we investigate if their progenitors could have provided sufficient ionizing photons to sustain the reionization. To maximize their contribution to the ionizing photon budget, we consider an extreme – probably unphysical – case where *all* such high-mass galaxies were formed at the same time at  $z_{\text{reion}}$ , which is the redshift when the reionization began.

The precise value of  $z_{\text{reion}}$  is still not known. Assuming instantaneous reionization with ionization fraction of  $x_e = 1$  at  $z < z_{\text{reion}}$ , Kogut et al. (2003) found  $z_{\text{reion}} = 17 \pm 3$  based on the first-year WMAP results. Allowing for uncertainties in the reionization history, Kogut et al. obtained  $11 < z_{\text{reion}} < 30$  (at 95% confidence level). The most recent, three-year WMAP results have refined this estimate, but the derived value of  $z_{\text{reion}}$  is still model-dependent (Spergel et al. 2006). Assuming that the reionization happened instantaneously at  $z > 7$ , they found the maximum-likelihood value of  $z_{\text{reion}} = 11.3$ . For the purpose of demonstration, we use  $z_{\text{reion}} = 9.0, 11.3$  and  $15.0$  as examples in the discussion below.

According to Madau, Haardt & Rees (1999; their Eqn. 27), the critical SFR density required to reionize the universe can be calculated as  $\rho_{\text{SFR}}^{\text{cri}}(z) \approx 0.013 f_{\text{esc}}^{-1} \times [(1+z)/6]^3 M_{\odot} \text{ yr}^{-1} \text{ Mpc}^{-3}$  (assuming a Salpeter IMF). This quantity, calculated by assuming  $f_{\text{esc}} = 0.1$ , is shown as the black, solid curves in Fig. 14 for the three assumed  $z_{\text{reion}}$  values. The contribution from the progenitors of the high-mass galaxies to the total SFR density depends on their SFH, and is less if the SFH is more prolonged. Fig. 14 shows the results for three toy models of exponentially declining SFHs with  $\tau$  of 0.1 (blue), 1.0 (green) and 10 Myr (red). The solid, dashed and dotted curves represent the results based on the minimum, representative and maximum global stellar mass densities shown in Fig. 12, respectively. These calculations demonstrate that, unless the bulk of their stars are *simultaneously* formed through an intense burst of very short duration ( $\tau \lesssim 10$  Myr), the contribution from the progenitors of the galaxies similar to those in our sample is not sufficient to reionize the universe. Even if they indeed came into being through an unphysically short, simultaneous burst with  $\tau \lesssim 10$  Myr, they cannot keep the universe ionized for long (only  $\lesssim 3$  Myr).

This is not to say, however, that star-forming galaxies cannot reionize the universe, because here we only count the progenitors of galaxies that have comparable stellar masses to those in our sample. If the MF has a very steep slope at the low-mass end, dwarf galaxies (which are below the detectability of our current observations) can contribute sufficient amount of ionizing photons, similar to the arguments made by Yan & Windhorst (2004a, b)

for the case at  $z \approx 6$ .

## 6. Summary

In this paper, we use the full-epoch IRAC observations of the GOODS *Spitzer* Legacy Program to study the stellar masses of galaxies at  $z \approx 6$ . In total, 53  $i_{775}$ -dropouts (seven of them with spectroscopic confirmation) selected in the entire GOODS fields ( $\sim 330$  arcmin $^2$ ) are securely detected by the IRAC. We derive the stellar masses for all these objects, using three different mass estimators:  $M_{\min}$ ,  $M_{\text{rep}}$ , and  $M_{\max}$ . We argue that the true mass of an object should be between  $M_{\min}$  and  $M_{\max}$ , and use  $M_{\text{rep}}$  as its “representative mass”. We further refer to the age to which  $M_{\text{rep}}$  corresponds as its “representative age”,  $T_{\text{rep}}$ . We find that the  $M_{\text{rep}}$  values range from  $0.09\text{--}7.0 \times 10^{10} M_{\odot}$ , and the  $T_{\text{rep}}$  values range from 50–400 Myr, both are consistent with the results of our earlier work based on a smaller sample in the HUDF (Paper I). We also study 79  $i_{775}$ -dropouts that are invisible from the IRAC observations, and find that they are generally one order of magnitude less massive than those detected by IRAC. Their ACS-to-IRAC colors are much bluer than those of the IRAC-detected ones, indicating that their luminosities are dominated by young population of unreddened stars with ages  $\lesssim 40$  Myr. We discuss various sources of uncertainty in the mass estimates, and find that most of our mass estimates are relatively robust.

We discuss a number of implications of our results. As in Paper I, we find that the existence of the most massive galaxies in our much enlarged sample can still be explained by at least one set of N-body simulations of the hierarchical paradigm. We derive a lower limit to the global stellar mass density at  $z \approx 6$ , and conclude that at least 0.2–1.1% of the total stellar mass in the local universe has been locked in stars by  $z \approx 6$ . As the most massive galaxies in our sample should have much larger SFRs in the past, we discuss the prospect of detecting their progenitors at  $z > 7$ . A near-IR survey covering a few hundred arcmin $^2$  to a depth of  $AB \sim 24.0$  mag can provide valuable constraints on the properties of such progenitors even in the case of a null detection. We also discuss how the progenitors of galaxies comparable to those in our sample could contribute in reionizing the hydrogen in the early universe, and conclude that such progenitors alone are not sufficient to sustain the reionization of the universe.

We thank the other members of the GOODS team who have contributed to the success of the observations and data analysis. We also thank our referee, Rodger Thompson, for his prompt and insightful referee report. We are grateful to Kentaro Nagamine for his up-to-date MF. We wish to thank Ivo Labbe for useful discussion. Support for this work, part

of the *Spitzer Space Telescope* Legacy Science Program, was provided by NASA through Contract Number 1224666 issued by the Jet Propulsion Laboratory, California Institute of Technology under NASA contract 1407. HY acknowledges the support from the NASA grant HST-GO-09780.03.

## REFERENCES

Bertin, E. & Arnouts, S. 1996, A&AS, 117, 393

Brinchmann, J. & Ellis, R. S. 2000, ApJ, 536, L77

Bouwens, R. J., et al. 2004, ApJ, 616, L79

Bouwens, R. J., Illingworth, G. D., Thompson, R. I., Franx, M. 2005, ApJ, 624, L5

Bruzual, A. G. & Charlot, S. 2003, MNRAS, 344, 1000 (BC03)

Calzetti, D., Armus, L., Bohlin, R. C., Kinney, A. L., Koomneef, J., & Storchi-Bergmann, T. 2000, ApJ, 533, 682

Chabrier, G. 2003, PASP, 115, 763

Chary, R., Stern, D. & Eisenhardt, P. R. M. 2005, ApJ, 635, L5

Chen, H.-W. & Marzke, R. O. 2004, ApJ, 615, 603

Cohen, J. G. 2001, AJ, 121, 2895

Cole, S., Lacey, C. G., Baugh, C. M., & Frenk, C. S. 2000, MNRAS, 319, 168

Dickinson, M., et al. 2000, ApJ, 531, 624

Dickinson, M., Paopvich, C., Ferguson, H. C., & Budavari, T. 2003, ApJ, 587, 25

Dickinson, M., et al. 2004, ApJ, 600, L99

Egami, E., et al. 2005, ApJ, 618, L5

Eyles, L. P., Bunker, A. J., Stanway, E. R., Lacy, M., Ellis, R. S., & Doherty, M. 2005, MNRAS, 364, 443

Fazio, G. G., et al. 2004, ApJS, 154, 10

Giavalisco, M., et al. 2004a, ApJ, 600, L93

Giavalisco, M., et al. 2004b, *ApJ*, 600, L103

Kaufman, M. 1976, *Ap&SS*, 40, 369

Kroupa, P. 2001, *MNRAS*, 322, 231

Kogut, A., et al. 2003, *ApJS*, 148, 161

Madau, P., Haardt, F., & Rees, M. J. 1999, *ApJ*, 514, 648

Madau, P., Pozzetti, L. & Dickinson, M. 1998, *ApJ*, 498, 106

Mobasher, B., et al. 2005, *ApJ*, 635, 832

Nagamine, K., Cen, R., Hernquist, L., Ostriker, J. P., & Springel, V. 2004, *ApJ*, 610, 45

Night, C., Nagamine, K., Springel, V., & Hernquist, L. 2006, *MNRAS*, 366, 705

Papovich, C., Dickinson, M., & Ferguson, H. C. 2001, *ApJ*, 559, 620

Partridge, R. B & Peebles, P. J. E. 1967, *ApJ*, 147, 868

Rudnick, G., et al. 2003, *ApJ*, 599, 847

Salpeter, E. E. 1955, *ApJ*, 121, 161

Shull, J. M. & Silk, J. 1979, *ApJ*, 234, 427

Sunyaev, R. A., Tinsley, B. M., & Meier, D. L. 1978, *ComAp*, 7, 183

Spergel, D. N., et al. 2003, *ApJS*, 148, 175

Spergel, D. N., et al. 2006, submitted to *ApJ* (astro-ph/0603449)

Stanway, E. R., et al. 2004a, *ApJ*, 604, L13

Stanway, E. R., Bunker, A. J., McMahon, R. G., Ellis, R. S., Treu, T., & McCarthy, P. J. 2004b, *ApJ*, 607, 704

Thompson, R. I., Storrie-Lombardi, L. J., Weymann, R. J., Rieke, M. J., Schneider, G., Stobie, E., Lytle, D. 1999, *AJ*, 117, 17

Thompson, R. I., et al. 2005, *AJ*, 130, 1

Vanzella, E., et al. 2006, submitted to *A&A* (astro-ph/0601367)

Werner, M. W., et al. 2004, *ApJS*, 154, 1

Yan, H., et al. 2004, ApJ, 616, 63

Yan, H., et al. 2005, ApJ, 634, 109 (Paper I)

Yan, H. & Windhorst, R. A. 2004a, ApJ, 600, L1

Yan, H. & Windhorst, R. A. 2004b, ApJ, 612, L93

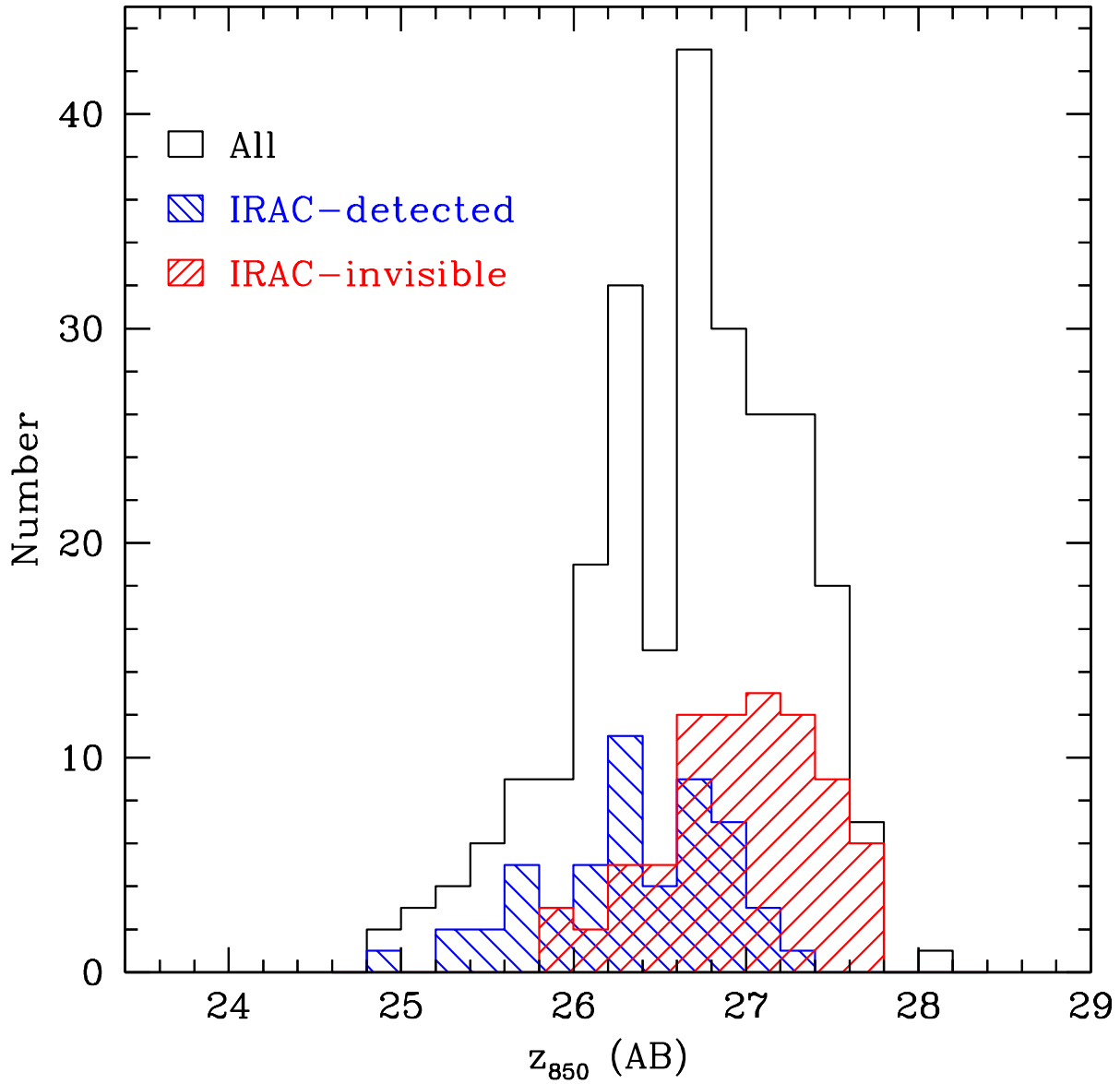


Fig. 1.— The distribution of  $z_{850}$  magnitudes of the  $i_{775}$ -dropouts in the GOODS fields. The shaded blue and red histograms are for the IRAC-detected and IRAC-invisible samples, respectively, while the black, unfilled histograms are for all objects (including the blended sample).

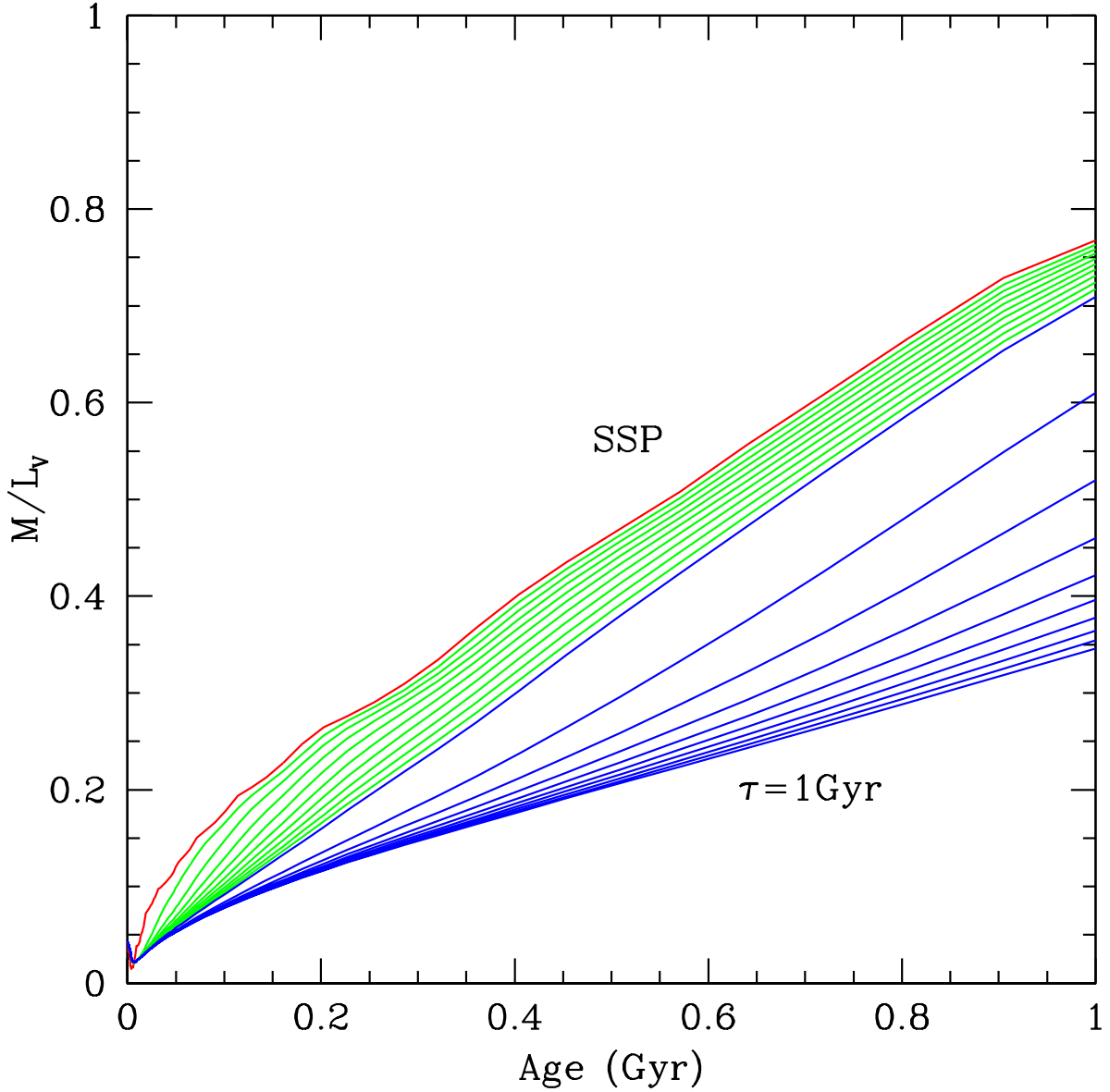


Fig. 2.— This figure demonstrates the evolution of mass-to-light-ratio ( $M/L$ ; shown here in terms of  $M/L_V$ ) for the models considered in our study (see §4). The red curve at the top corresponds to a SSP, the green curves correspond to models with  $\tau$  ranging from 10 to 90 Myr, while the blue curves correspond to models with  $\tau$  from 0.1 to 1.0 Gyr. At the age of  $\sim 1$  Gyr, which is the maximum age allowed by our adopted cosmology, a SSP reaches the largest possible  $M/L$  among all the models, and thus gives the highest possible stellar mass for a given luminosity.

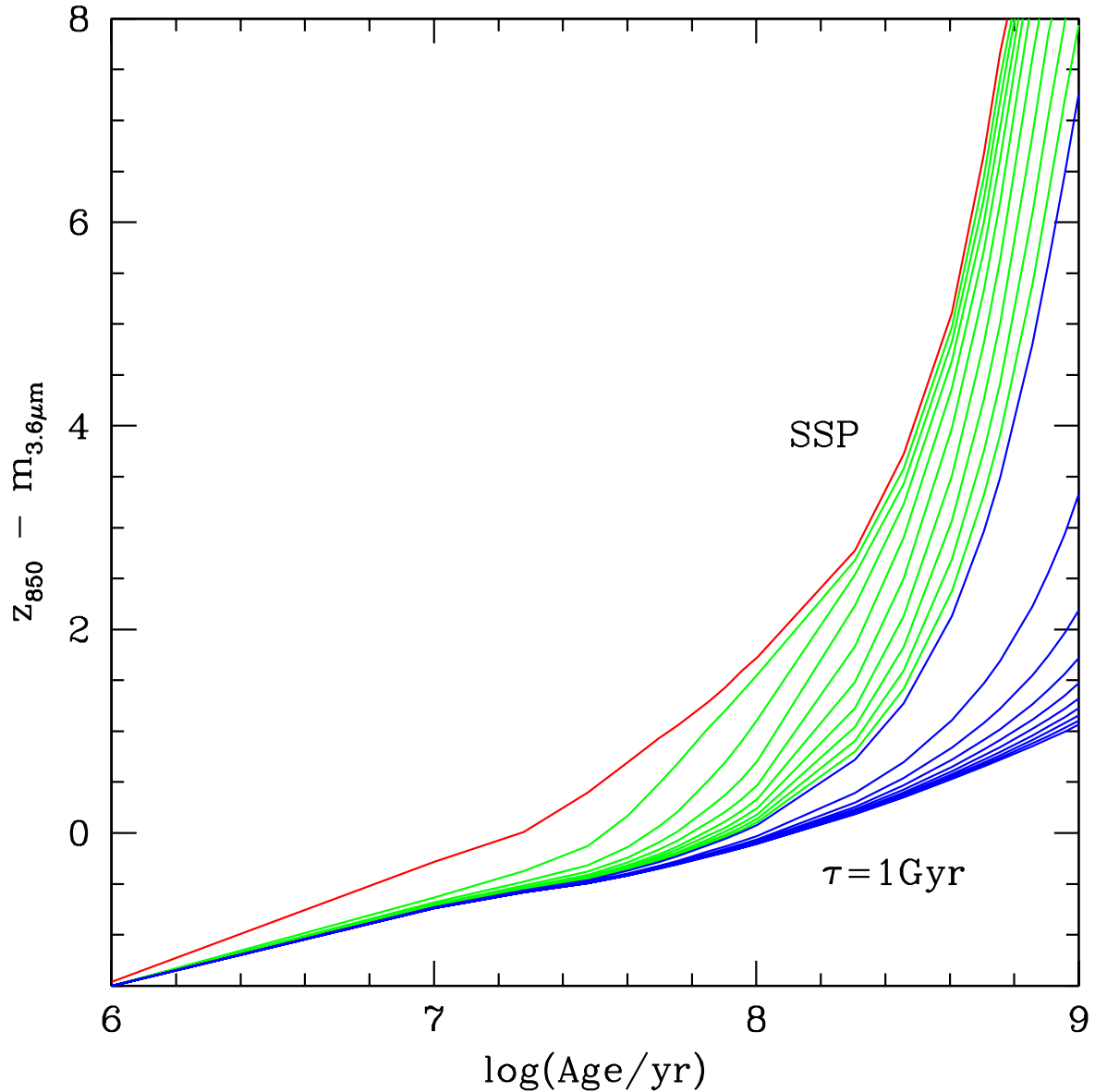


Fig. 3.— The evolution of  $(z_{850} - m_{3.6\mu\text{m}})$  color for the models considered in our study (see §4). The curves are color-coded in the same way as in Fig. 2. The  $(z_{850} - m_{3.6\mu\text{m}})$  color can be used as an age indicator.

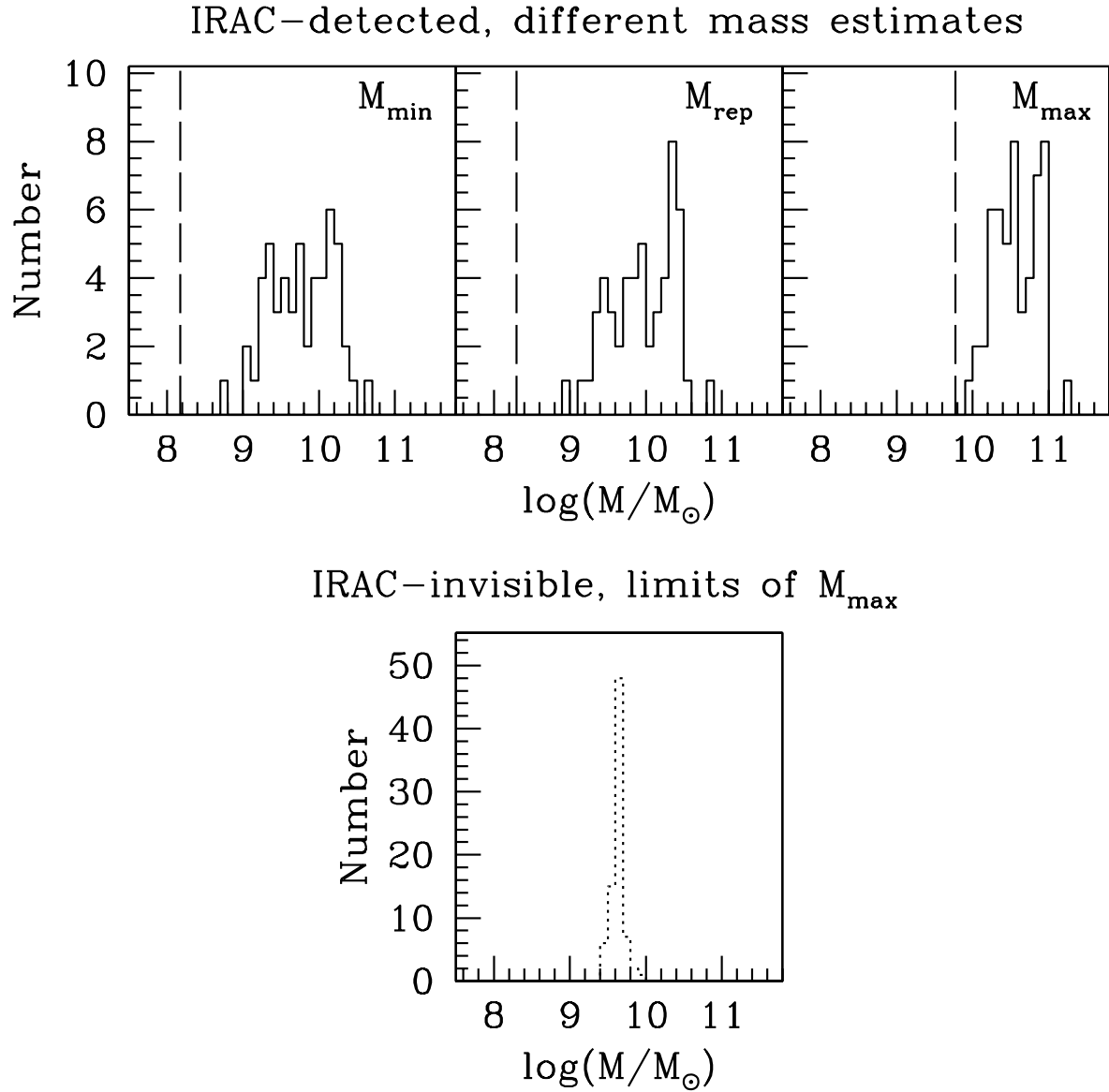


Fig. 4.— The top panel displays the histograms of the stellar mass estimates of the galaxies in the IRAC-detected samples, using three different estimators as described in §4.1. The vertical dashed line in each figure represents the corresponding mass estimate of a typical object in the IRAC-invisible sample (see §4.2). The bottom panel shows the histogram of the upper limits of the stellar masses of the galaxies in the IRAC-invisible sample, calculated using their flux density upper limits ( $2\sigma$ ) in the  $3.6\mu\text{m}$ -channel (see §4.2).

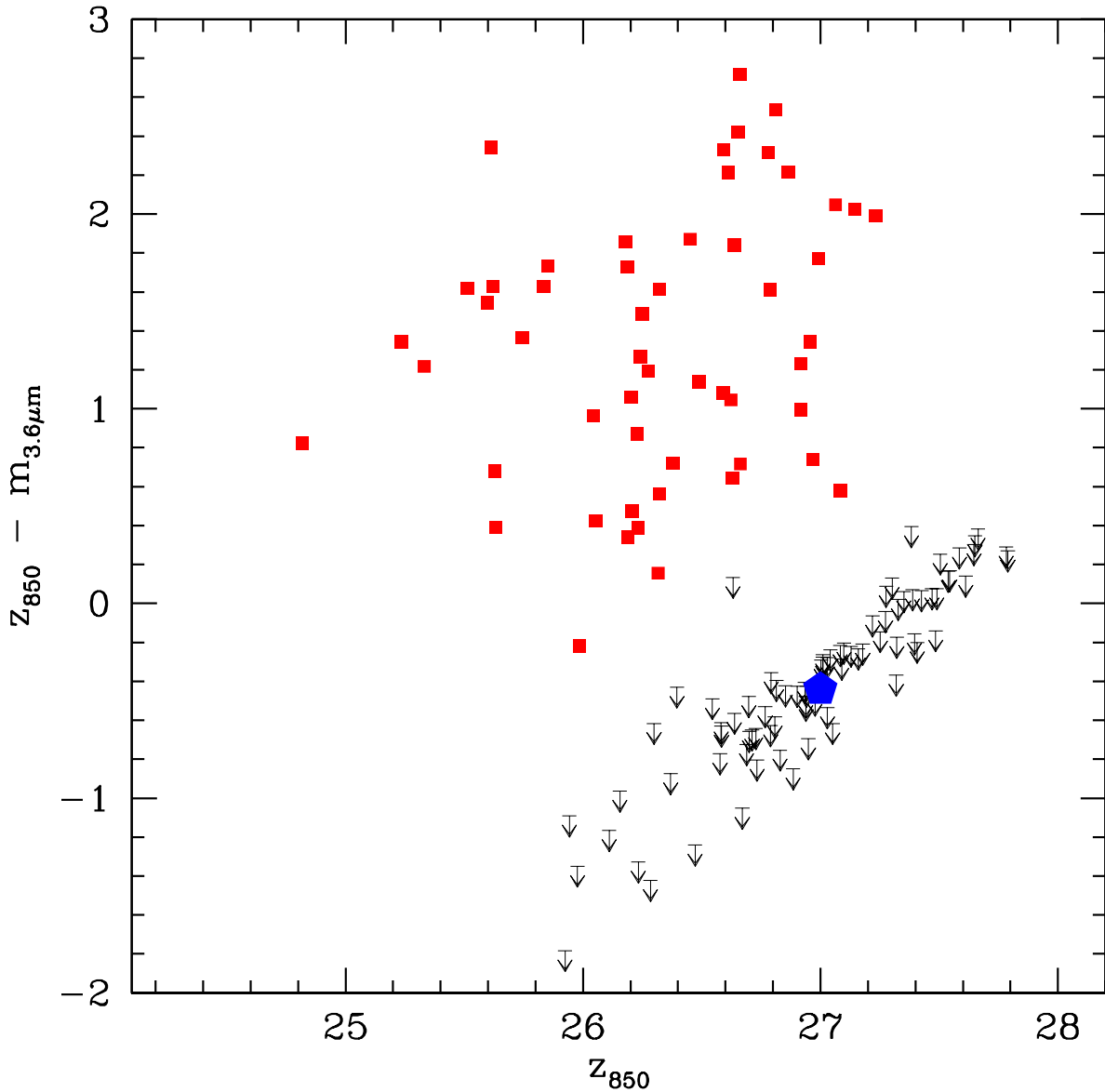


Fig. 5.— The  $(z_{850} - m_{3.6\mu m})$  colors of the IRAC-detected objects are shown as red solid squares, while the upper limits of these colors of the IRAC-invisible objects are shown as downward arrows. The blue hexagon represents the median color of the IRAC-invisible objects, which is calculated by using the median  $z_{850}$  magnitude of the sample and the  $m_{3.6\mu m}$  magnitude of the median stack. The IRAC-invisible objects are significantly bluer than the IRAC-detected ones, indicating that the young populations are playing a more important role in them than in the IRAC-detected objects.

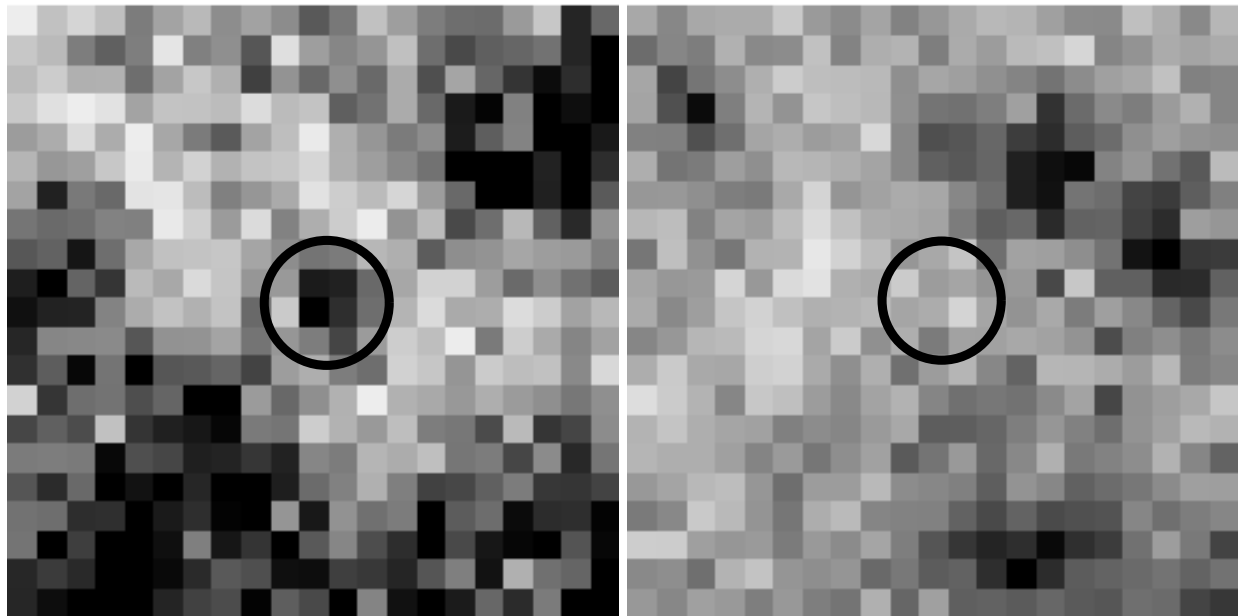


Fig. 6.— The  $3.6\mu\text{m}$  median stack of the objects in the IRAC-invisible sample is displayed in the left panel, where there is a visible source in the middle (indicated by the circle). For comparison, the median stacks of the same number of random positions is shown in the right panel and shows no detected source in the middle circle.

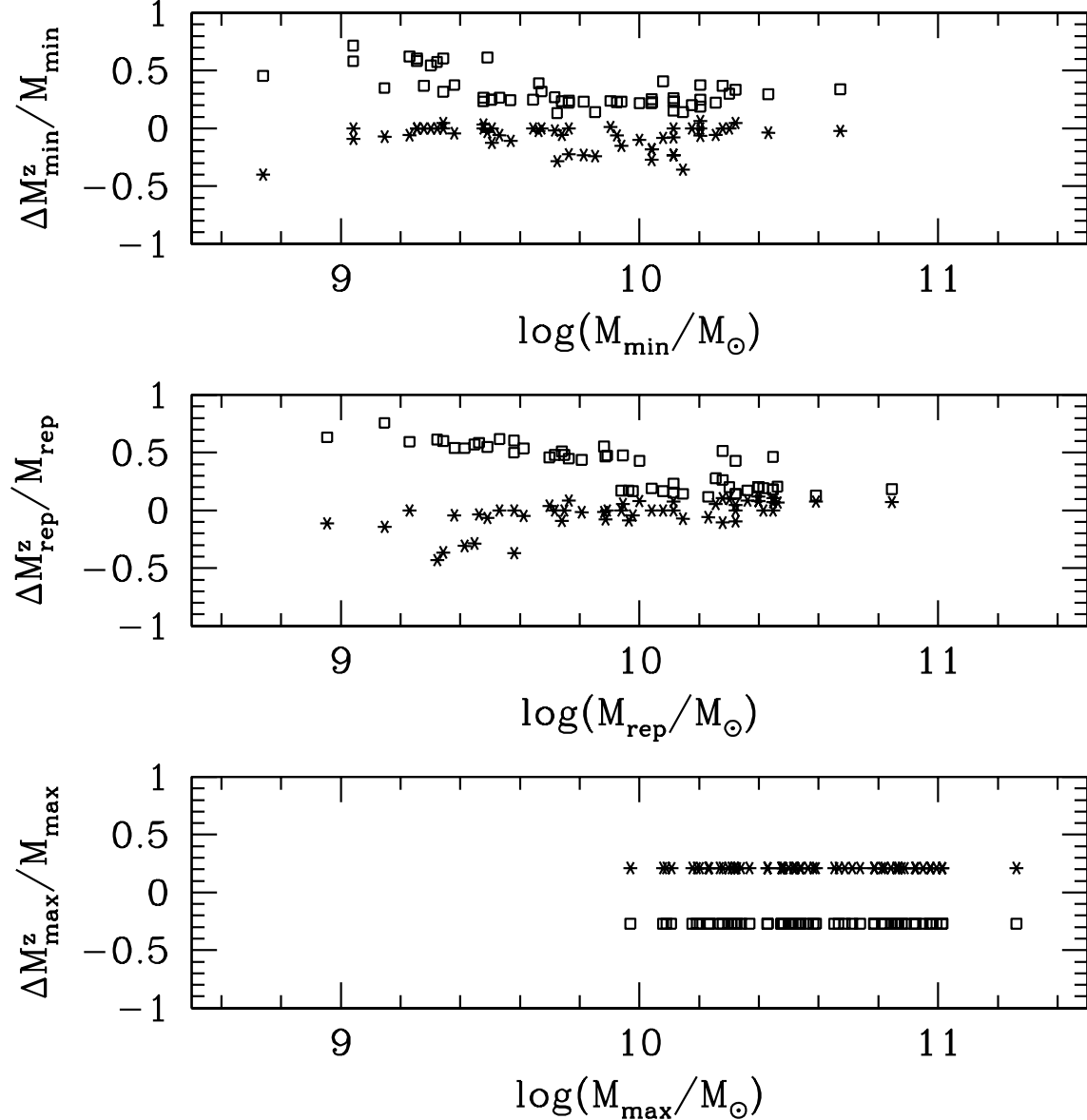


Fig. 7.— The systematic uncertainties of the stellar mass estimates caused by fixing the redshifts of our models at  $z = 6$ . The evaluations of the three mass estimates are repeated for every IRAC-detected object by using models at  $z = 5.5$  (asterisks) and  $z = 6.5$  (squares). The systematics are expressed in terms of relative differences of  $M_{\min}$ ,  $M_{\text{rep}}$  and  $M_{\max}$  in the top, middle and bottom panels, respectively. We define  $\Delta M^z = M - M'$ , where  $M$  is the value obtained with the original models at  $z = 6$ , and  $M'$  is the value obtained with the new models. Thus a positive data point means that our original evaluation overestimates the quantity if the object is actually at a redshift different from  $z = 6$ , and a negative data point means the opposite. If our objects are actually all at  $z = 5.5$ , our original results underestimate  $M_{\min}$  and  $M_{\text{rep}}$  only by a few percent on average, but overestimate  $M_{\max}$  by 21%. If our objects are actually all at  $z = 6.5$ , our original results overestimate both  $M_{\min}$  and  $M_{\text{rep}}$  by  $\sim 25\%$ , and underestimate  $M_{\max}$  by 27%.

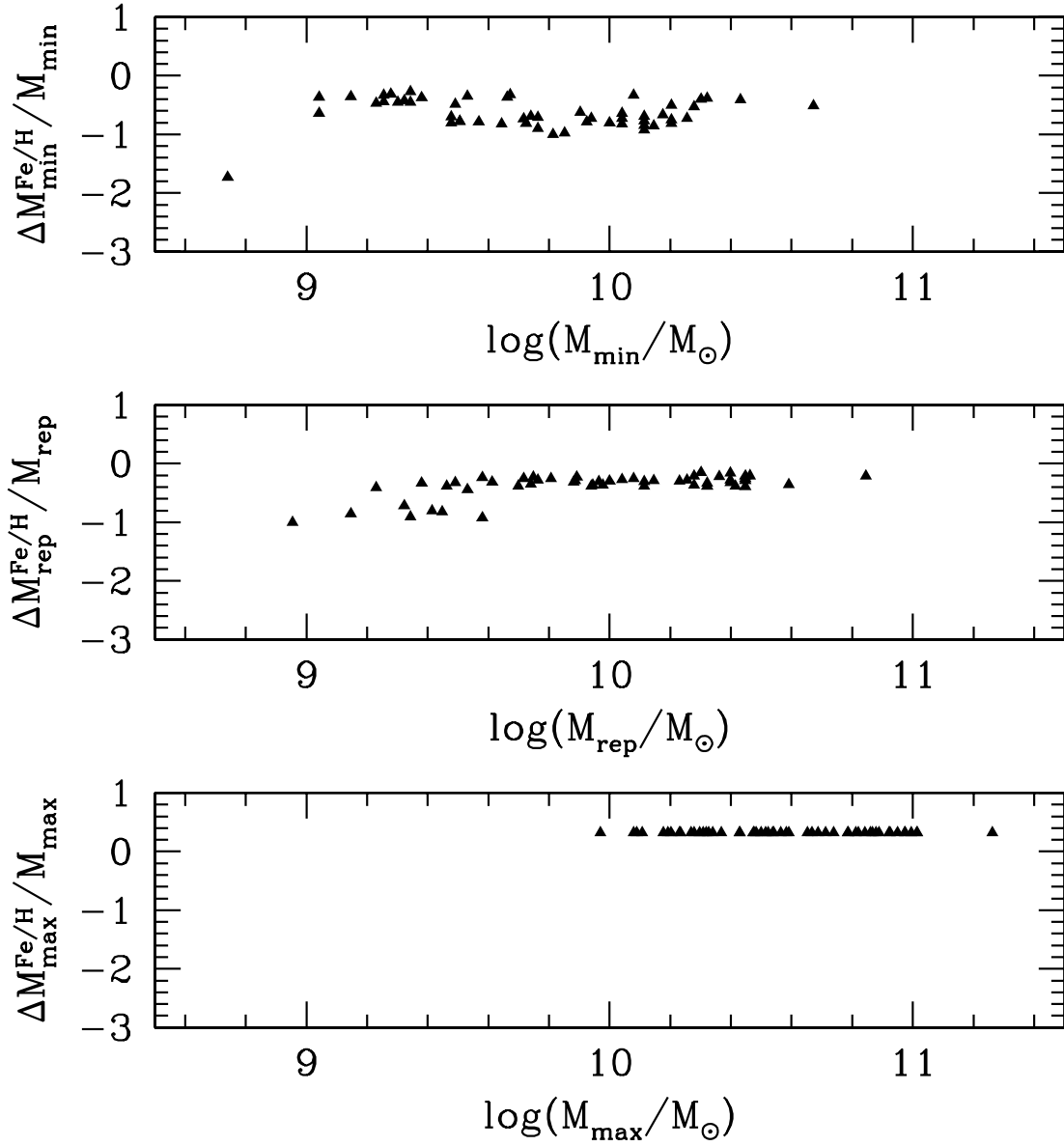


Fig. 8.— Similar to Fig. 7, but for the systematic uncertainties caused by using models of solar metallicity only. The mass estimates are recalculated by using models with metallicity of 1/200 of solar, which is the lowest abundance available for the BC03 models. The relative difference of mass is defined in a similar way to the quantity shown in Fig. 8. If all our objects actually have such a low metallicity, our original results underestimate  $M_{\min}$  and  $M_{\text{rep}}$  by  $\sim 70\%$  and  $32\%$  on average, respectively, and overestimate  $M_{\max}$  by  $32\%$ .

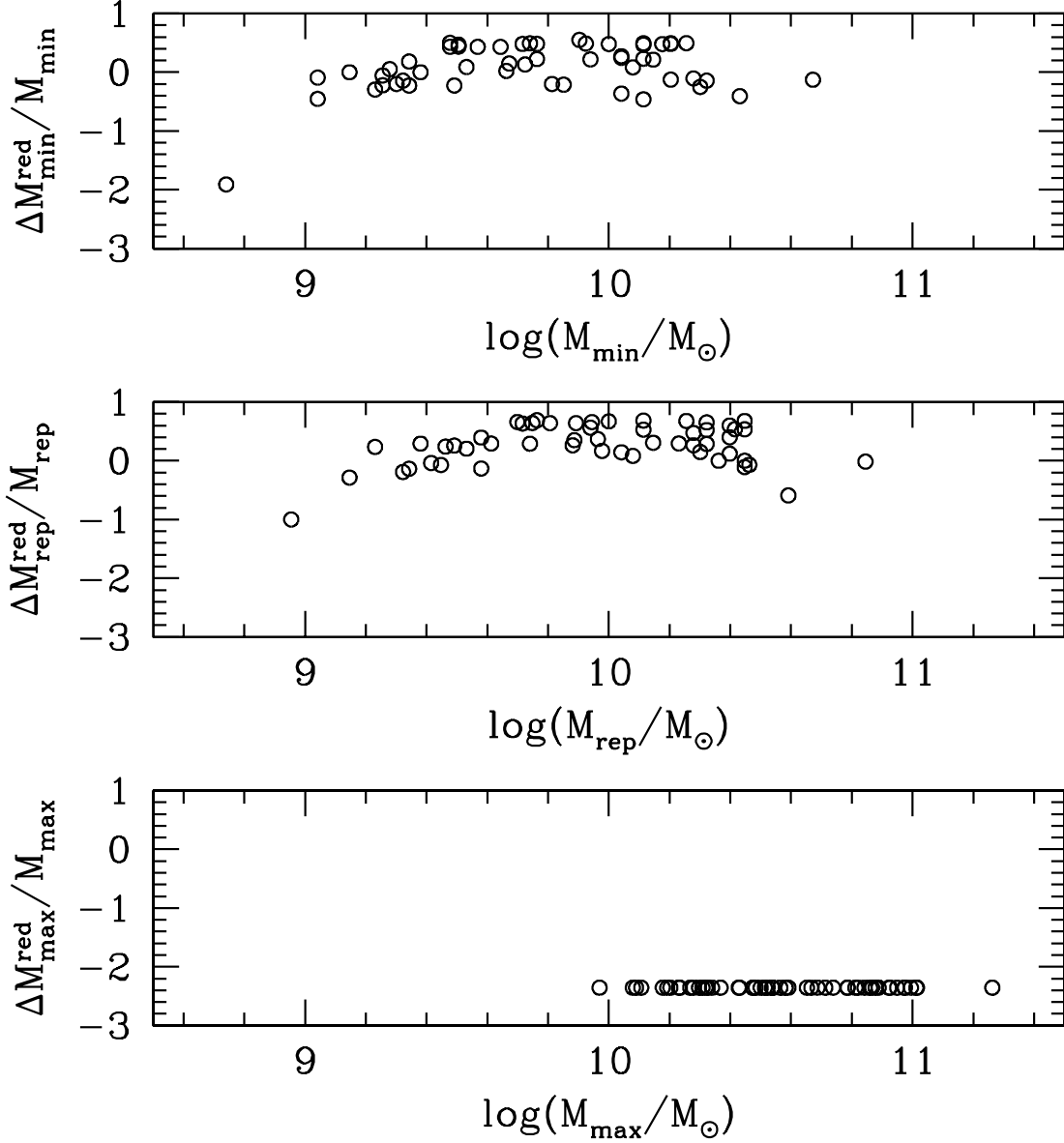


Fig. 9.— Similar to Fig. 7 and 8, but for the systematic uncertainties caused by using zero-reddening models. The mass estimates are recalculated by using models with  $E(B-V) = 0.2$  mag, following the reddening law of Calzetti et al. (2000). The relative difference of mass is defined in a similar way as before. If all our objects actually suffer from dust reddening and obscuration of this amount, our original results overestimate  $M_{\min}$  and  $M_{\text{rep}}$  by  $\sim 13\%$  and  $30\%$ , respectively, and underestimate  $M_{\max}$  by  $\sim$  a factor of 3.35.

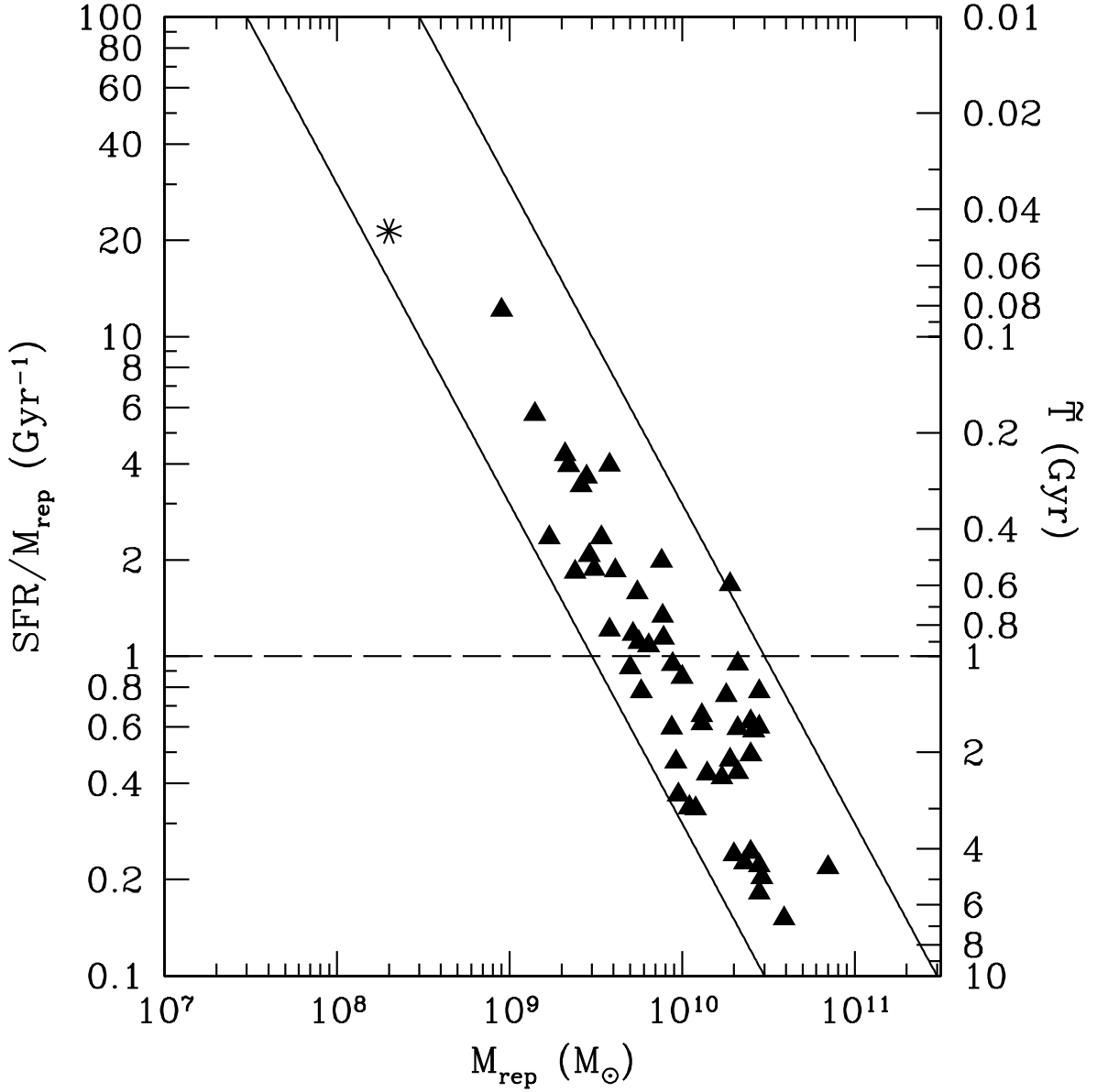


Fig. 10.— The specific SFRs of the IRAC-detected objects (filled triangles) as a function of  $M_{\text{rep}}$ . For completeness, the specific SFR of the IRAC-invisible objects, calculated using their median  $z_{850}$  magnitudes and the median  $3.6\mu\text{m}$  stack, is also shown (the asterisk). The two solid lines shows the specific SFRs of objects with constant SFRs of 3.0 (left) and  $30 M_{\odot} \text{ yr}^{-1}$  (right). The label to the right shows the time periods through which the galaxies can assemble their total masses if their past SFRs are the same as the current values. The horizontal dashed line indicates the age of the universe at  $z \approx 6$ . Objects below this line must have acquired their masses at a much higher SFR than the current values.

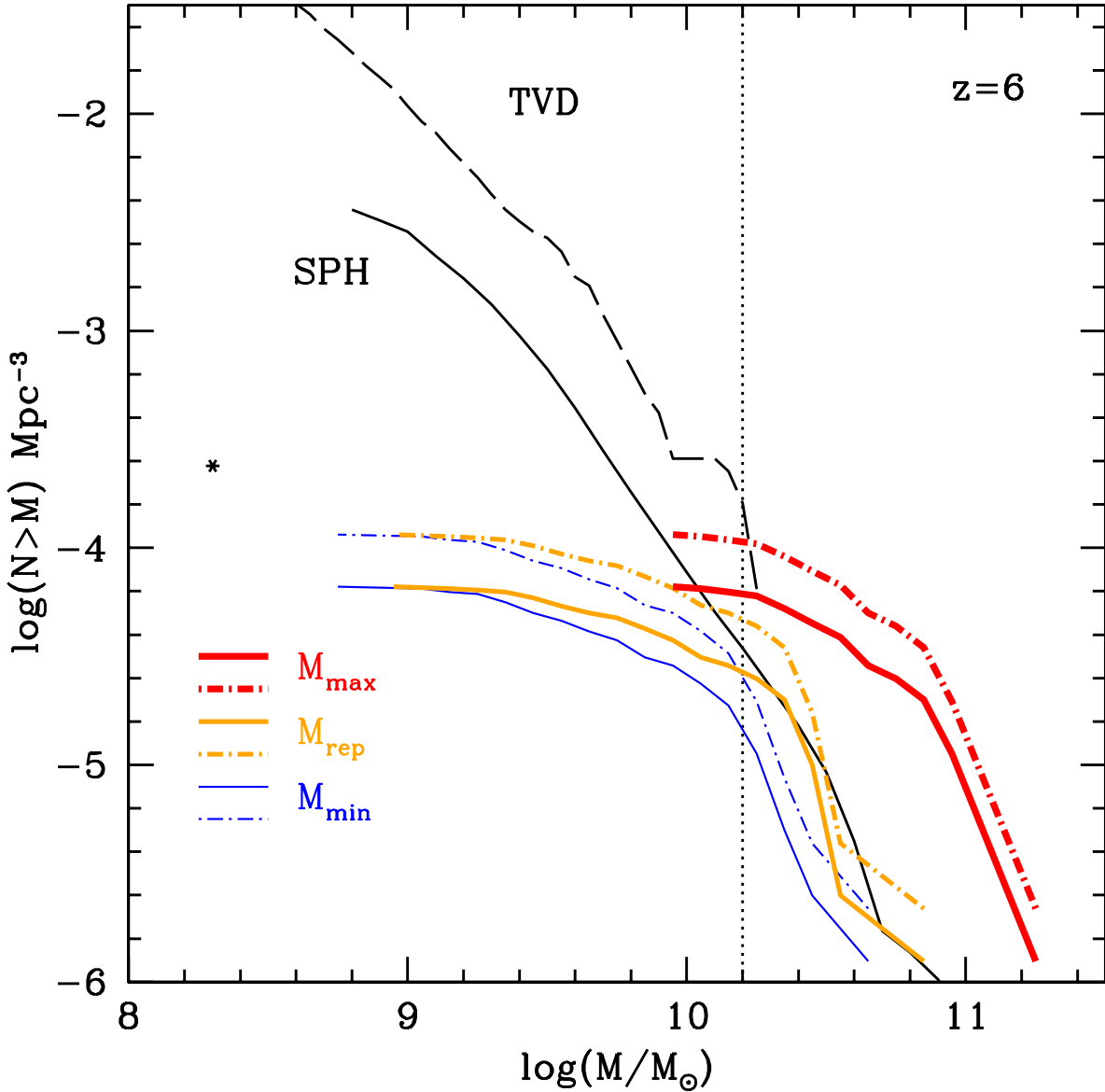


Fig. 11.— The comparison between the observed number density inferred from our sample and the mass functions predicted by a set of N-body hydrodynamic simulations in a  $\Lambda$ CDM universe from Nagamine et al. (2004) and Night et al. (2006). Both are presented as cumulative number densities. The simulations are shown as the black solid (SPH) and dashed (TVD) curves, while the observed number densities based on ( $M_{\min}$ ,  $M_{\text{rep}}$ ,  $M_{\max}$ ) are shown as the blue, yellow and red curves, respectively. The solid, color-coded curves are the observed values based only on the non-blended, IRAC-detected sample, while the dot-dashed, color-coded curves are those after taking the blended sample into account. The asterisk to the left is the observed cumulative density when assuming all the IRAC-invisible objects (after correction for blending) have the  $M_{\text{rep}}$  value as derived using the median stack (see §4.2). The dotted vertical line at ( $M = 1.6 \times 10^{10} M_{\odot}$ ) indicates the mass threshold above which our IRAC data (but not necessarily the  $i_{775}$ -dropout sample itself) are complete.

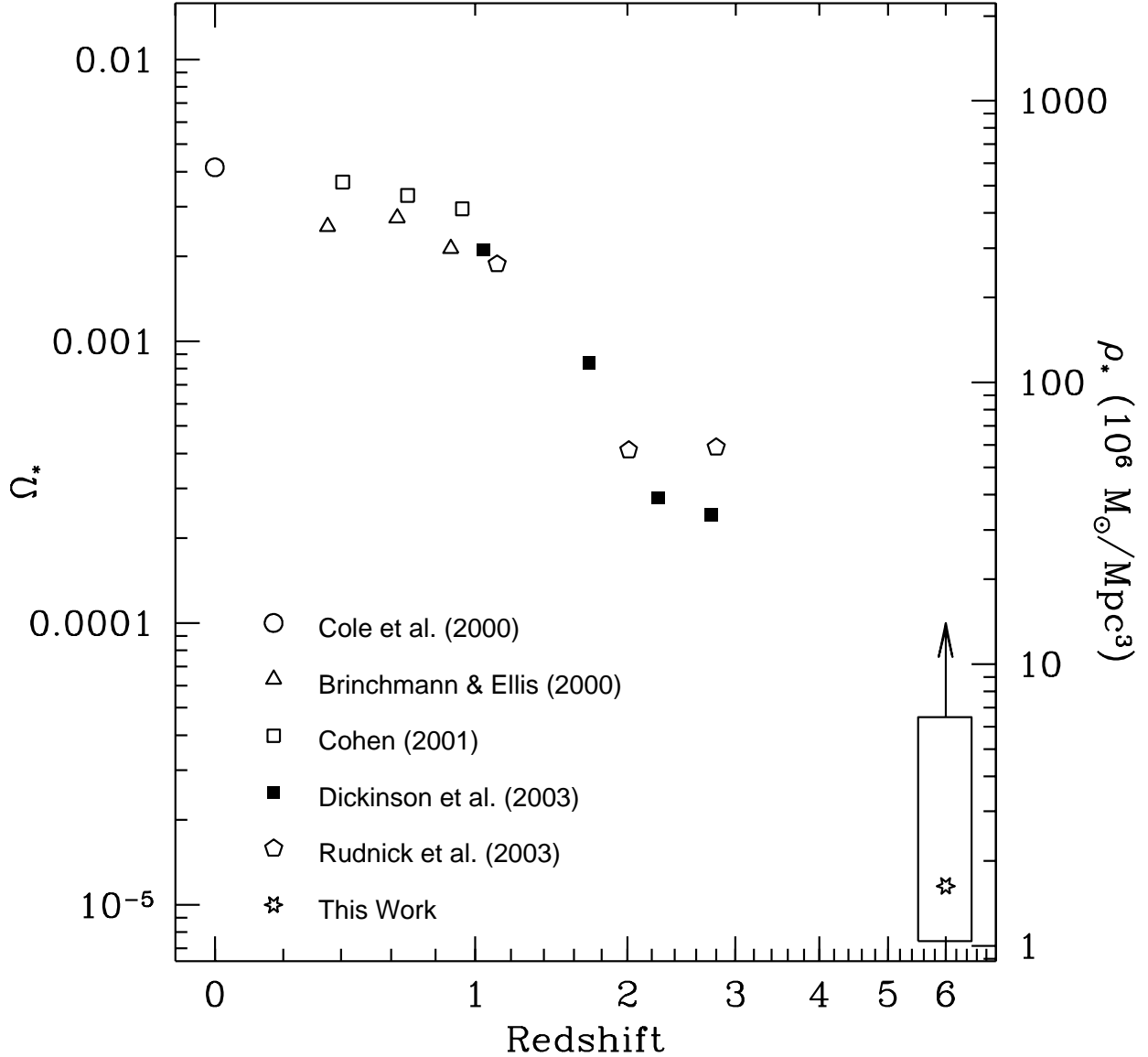


Fig. 12.— The lower limit to the global stellar mass density at  $z \approx 6$  based on our study is shown as the rectangle in this figure. The open star inside this rectangle shows the result based on the  $M_{rep}$  values, while the lower and upper boundaries are set based on the  $M_{min}$  and  $M_{max}$  values, respectively. The upward arrow indicates that these results are lower limits. The results at lower redshifts are from Cole et al. (2000), Brinchmann & Ellis (2000), Cohen (2001), Dickinson et al. (2003) and Rudnick et al. (2003). The Y-axis labels to right are in unit of  $M_\odot/Mpc^3$ , while the ones to the left are in terms of ratio to the critical mass density, which is  $1.4 \times 10^{11} M_\odot Mpc^{-3}$  for our adopted cosmology.

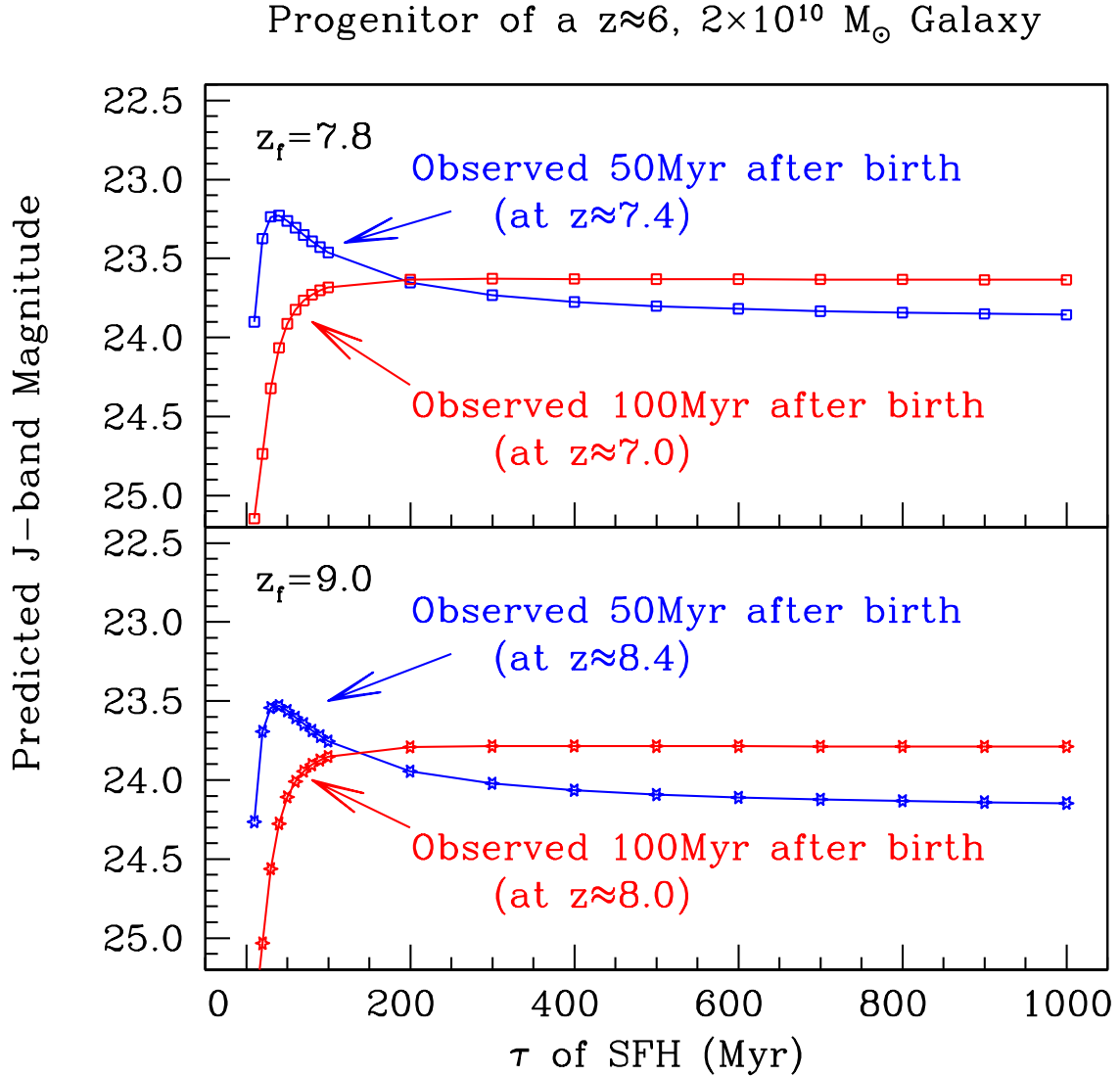


Fig. 13.— The predicted  $J$ -band brightness of the progenitor of a typical high-mass object ( $M = 2 \times 10^{10} M_\odot$ ) in the IRAC-detected sample. The brightness depends on how quickly the progenitor has been forming stars (characterized by the timescale  $\tau$  of the exponential SFH) and when it is observed after its birth. Two cases, 50 and 100 Myr after the birth, are shown as the blue and red curves, respectively. With a formation redshift of  $z_f = 7.8$  (top panel), these two ages correspond to being observed at  $z \approx 7.4$  and 7.0, respectively, while with a formation redshift of  $z_f = 9.0$  (bottom panel), they correspond to being observed at  $z \approx 8.4$  and 8.0, respectively. These two formation redshifts are chosen for demonstration because a galaxy evolving to  $z \approx 6$  would have an age of 200–400 Myr, which spans the  $T_{\text{rep}}$  range of the  $M > 10^{10} M_\odot$  objects in the IRAC-detected sample. The calculation is done for  $\tau = 10$  Myr to 1 Gyr based on the BC03 models, assuming no dust extinction. A modest amount of dust corresponding to  $E(B - V) \approx 0.2$  mag would lower the brightness by  $\sim 2$  mag.

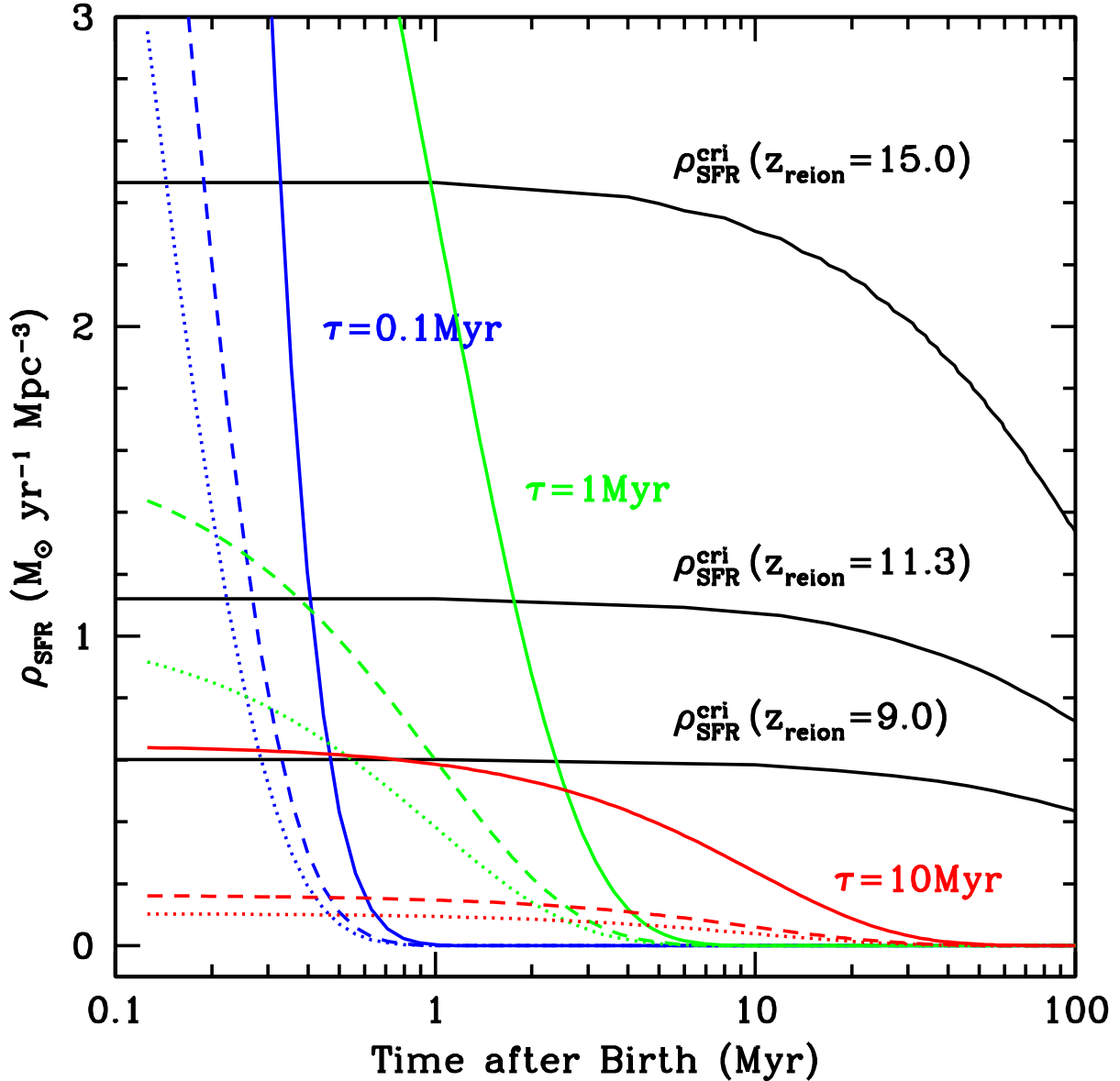


Fig. 14.— The contribution to the reionizing photon background by primeval galaxies, inferred from the progenitors of the objects in our sample. We assume an extreme case where the universe started to give birth to all the progenitors of the galaxies in our sample at the same time at  $z_{\text{reion}}$ , and show the contribution of these progenitors to the reionizing photon background, expressed in terms of SFR density, as a function of time after the birth. This contribution is very sensitive to the SFH of the galaxies. Here we show the results for three exponentially declining SFHs with  $\tau$  of 0.1, 1.0 and 10 Myr as blue, green and red curves, respectively. The solid, dashed and dotted curves represent the results that correspond to the minimum, representative and maximum global stellar mass densities shown in Fig. 12, respectively. The black curves, corresponding to  $z_{\text{reion}} = 15.0, 11.3$  and  $9.0$ , are the critical SFR densities needed to fully ionize the neutral hydrogen in the universe, calculated according to Madau, Haardt & Rees (1999). See §5.2 for detailed interpretation.